

THESIS FOR THE DEGREE OF DOCTOR OF PHILOSOPHY

STRUCTURE-FUNCTION RELATIONSHIPS IN Ru<sup>II</sup> COMPLEXES WITH  
UNCONVENTIONAL LIGANDS

PHOTOPHYSICAL AND PHOTOCHEMICAL STUDIES

JOACHIM WALLENSTEIN



Department of Chemistry and Chemical Engineering  
CHALMERS UNIVERSITY OF TECHNOLOGY

Gothenburg, Sweden, 2016

Structure-Function Relationships in Ru<sup>II</sup> Complexes with Unconventional Ligands:  
Photophysical and Photochemical Studies  
Joachim Wallenstein  
ISBN: 978-91-7597-378-4

© Joachim Wallenstein, 2016.

Doktorsavhandlingar vid Chalmers tekniska högskola  
Ny serie Nr 4059  
ISSN: 0346-718X

Department of Chemistry and Chemical Engineering  
Chalmers University of Technology  
SE-412 96 Gothenburg  
Sweden  
Telephone: +46 (0)31 772 1000

**Front cover:** Illustration of selected ligands used in Ru<sup>II</sup> complexes in the thesis.

**Back cover:** Photo of the author. © Joachim Wallenstein, 2015

Printed by Chalmers Reproservice  
Gothenburg, Sweden, 2016

# STRUCTURE-FUNCTION RELATIONSHIPS IN Ru<sup>II</sup> COMPLEXES WITH UNCONVENTIONAL LIGANDS

PHOTOPHYSICAL AND PHOTOCHEMICAL STUDIES

JOACHIM WALLENSTEIN

Department of Chemistry and Chemical Engineering  
Chalmers University of Technology

## ABSTRACT

The rich photophysics, photochemistry and electrochemistry of Ru<sup>II</sup> complexes have attracted intense research interest in widely disparate fields. A large portion of the studied and applied complexes are derived from the archetypical [Ru(bpy)<sub>3</sub>]<sup>2+</sup> (bpy is 2,2'-bipyridine), which absorbs in the visible region, displays a long lived (~1 μs), emissive metal-to-ligand charge transfer state, and shows reversible electrochemistry in both the ground and excited state. Adding substituents to the bpy ligand is a conventional way of fine-tuning the physical properties. Incorporating larger motifs, altering the coordination sphere geometry or coordinating ligands via other heteroatoms than nitrogen can result in substantially different physical properties. This latter approach is the subject of this thesis, and in it I have presented the results from studies on structure complexes incorporating what I chose to call unconventional ligands. This thesis is focused on the structure-function relationships in three series of Ru<sup>II</sup> complexes:

- 1) With strained bpy-ligands, connected in the 3,3'-positions, with electron rich dithiol-motifs that display high light harvesting capabilities. Additionally, they promote hole-transfer when used for sensitizing a semiconductor substrate, with long-lived charge separated states.
- 2) Pyridine-thioether complexes that display excited state properties on par with [Ru(bpy)<sub>3</sub>]<sup>2+</sup> and pyridine-sulfoxide complexes that display two-color reversible photo-isomerization in solution and immobilized on a semiconductor substrate.
- 3) Quinoline-pyrazole ligands that when coordinated form near perfect octahedral complexes; two of which display different selectivity toward photo-chlorination with respect to Cl<sup>-</sup> source, and one that displays room temperature dynamic diastereomerization in the ground state while at the same time being extremely photo-stable.

**Keywords:** Ru<sup>II</sup> complexes, structure-function relationship, photochemistry, spectral component analysis, hole-transfer, photoreaction

## LIST OF PUBLICATIONS

The thesis is based on the following publications and manuscripts, referred to by Roman numerals in the text:

- I. High Extinction Coefficient Ru-Sensitizers that Promote Hole Transfer on Nanocrystalline TiO<sub>2</sub>  
Maria Abrahamsson, Joachim H.J. Hedberg, Hans-Christian Becker, Aaron Staniszewski, Wayne H. Pearson, William B. Heuer, Gerald J. Meyer  
*ChemPhysChem*, **2014**, 15, 1154-1163
- II. Emissive Ruthenium-Bisdiimine Complexes with Chelated Thioether Donors  
Joachim Hedberg Wallenstein, Jonas Sundberg, Christine J. McKenzie, Maria Abrahamsson  
*Eur. J. Inorg. Chem.*, **2016**, 6, 897-906
- III. Two-color photo-induced linkage isomerism in a Ru-sulfoxide complex in solution and immobilized on nanocrystalline TiO<sub>2</sub>  
Joachim Hedberg Wallenstein, Fredrik Johansson, Jerker Mårtensson, Maria Abrahamsson  
*Manuscript*
- IV. A Homoleptic Trisbidentate Ru(II) Complex of a Novel Bidentate Biheteroaromatic Ligand Based on Quinoline and Pyrazole Groups: Structural, Electrochemical, Photophysical, and Computational Characterization  
Martin Jarenmark, Lisa A. Fredin, Joachim H.J. Hedberg, Isa Doverbratt, Petter Persson, Maria Abrahamsson  
*Inorg. Chem.*, **2014**, 53, 12778-12790
- V. Diastereoisomerization Dynamics of a Bistridentate Ru<sup>II</sup> Complex  
Martin Jarenmark, Göran Carlström, Lisa A. Fredin, Joachim Hedberg Wallenstein, Isa Doverbratt, Maria Abrahamsson, Petter Persson  
*Inorg. Chem.*, **2016**, 55, 3015-3022
- VI. Chemical Consequences of Pyrazole Orientation: Ru<sup>II</sup> Complexes of Unsymmetrical Quinoline-Pyrazole Ligands  
Joachim Hedberg Wallenstein, Lisa A. Fredin, Martin Jarenmark, Petter Persson, Maria Abrahamsson, Petter Persson  
*Submitted to Dalton Transactions*
- VII. Excited State Dynamics in Ru<sup>II</sup> Complexes of Quinoline-Pyrazole Ligands  
Joachim Hedberg Wallenstein, Lisa A. Fredin, Martin Jarenmark, Petter Persson, Maria Abrahamsson  
*Manuscript*

## MY CONTRIBUTION

Note: I previously carried the family name Hedberg.

In Paper I, I carried out the measurements at 80 K and molar absorptivities of ligands. In Paper II, III, IV, VI and VII, I planned and performed all the optical spectroscopic and electrochemical measurements (excluding a UV-Vis-coupled <sup>1</sup>H-NMR experiment). My contribution to Paper V have been in the discussion and writing of the paper. I have been participating in the writing of all manuscripts, been involved in discussion, and been the lead author in Paper II, III, VI and VII.

# TABLE OF CONTENTS

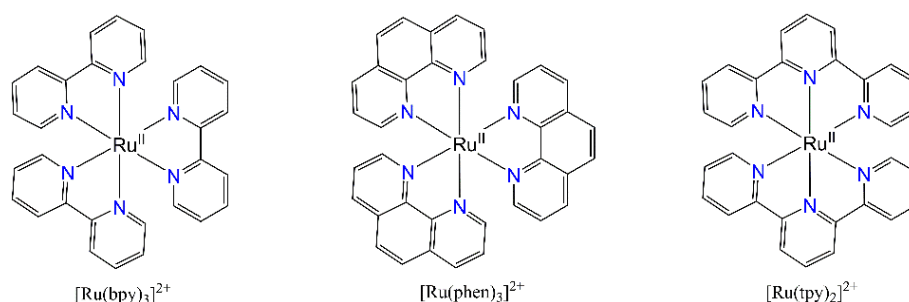
<b>1. Introduction</b>	<b>1</b>
<b>2. Background</b>	<b>5</b>
2.1. Photophysics and Photochemistry	5
2.1.1. <i>Light-matter interactions</i>	5
2.1.2. <i>Photophysical processes</i>	8
2.1.3. <i>Photochemical reactions</i>	10
2.1.4. <i>Quantum yields and rates of photoinduced processes</i>	10
2.1.5. <i>Non-linear optical effects.</i>	12
2.2. Electron Transfer	12
2.3. Ru <sup>II</sup> complexes	14
2.3.1. <i>Electronic structure of archetypical RuII complexes</i>	14
2.3.2. <i>Structural influences on the excited state manifold</i>	16
2.3.3. <i>Diastereomerism and induced isomerization</i>	17
<b>3. Methods and techniques</b>	<b>19</b>
3.1. Absorption spectroscopy	19
3.1.1. <i>Steady state absorption spectroscopy</i>	19
3.1.2. <i>Absorption-coupled Photolysis</i>	19
3.1.3. <i>Transient absorption spectroscopy</i>	19
3.2. Emission spectroscopy	20
3.2.1. <i>Steady state emission spectroscopy.</i>	20
3.2.2. <i>Time resolved emission spectroscopy.</i>	21
3.3. Relative actinometry	22
3.3.1. <i>Emission quantum yields</i>	22
3.3.2. <i>Quantum yield of photochemical reactions</i>	22
3.4. Electrochemistry	22
3.5. Data analysis	23
3.5.1. <i>Excited state decay fitting</i>	22
3.5.2. <i>Spectral component analysis.</i>	23
<b>4. Results and discussions</b>	<b>25</b>
4.1. Coordinating 3,3'-connected ligands	25
4.1.1. <i>Structures</i>	25

4.1.2. Absorption and electrochemical properties	26
4.1.3. Excited state properties	27
4.1.4. Short summary	29
4.2. Coordinating sulfur-donating ligands	30
4.2.1. Structures	30
4.2.2. Absorption and electrochemical properties	31
4.2.3. Excited state properties	33
4.2.4. Short summary	37
4.3. Coordinating quinoline-pyrazole ligands	38
4.3.1. Structures	38
4.3.2. Absorption and electrochemical properties	40
4.3.3. Excited state properties	41
4.3.4. Short summary	45
<b>5. Concluding remarks</b>	<b>47</b>
<b>6. Acknowledgements</b>	<b>51</b>
<b>7. References</b>	<b>53</b>
<i>Appended papers I-VII</i>	

# 1. Introduction

Transition metals are commonly coordinated with small organic molecules, so called ligands, to form transition metal complexes. The complexes exhibit several properties that differs from organic molecules. One advantage with metals is the relatively narrow potential range of the different oxidation states, (such as  $M^{\text{II}}$ ,  $M^{\text{III}}$ ,  $M^{\text{IV}}$  ...). Additionally, the large number of coordination sites compared to lighter atoms allows for more complex structures with unique properties. This is the basis for a lot of the chemical applications of transition metal complexes. In this thesis, I have studied such complexes based on ruthenium, and the photophysical, photochemical and electrochemical properties arising from coordinating ligands, and the connection between structure and function.

In 1959 the first report on the long lived charge transfer photoluminescence of  $[\text{Ru}(\text{bpy})_3]^{2+}$  (bpy = 2,2'-bipyridine) was published by Paris and Brandt, Scheme 1.<sup>1</sup> Following the publication, enormous amounts of research hours have been invested in  $[\text{Ru}(\text{bpy})_3]^{2+}$  and structurally similar transition metal complexes to scrutinize the nature of charge-transfer transitions and possible uses thereof.<sup>2-15</sup> Among these,  $\text{Ru}^{\text{II}}$  complexes have received the lion's share of attention,<sup>16</sup> in short because of a favorable energy level distribution upon coordination of the bpy-type ligands. This often results in prominent absorption in the visible region, long lived photoluminescence, and several other attractive properties, *vide infra*, which are not observed in most other transition metal complexes.



**Scheme 1.** Structure of  $[\text{Ru}(\text{bpy})_3]^{2+}$ ,  $[\text{Ru}(\text{phen})_3]^{2+}$ , and  $[\text{Ru}(\text{tpy})_2]^{2+}$ .

Now, more than half a century after Paris and Brandt's publication, innumerable mononuclear  $\text{Ru}^{\text{II}}$  complexes with chromophoric<sup>a,17</sup> ligands have been synthesized<sup>16, 18, 19</sup> (from here on,  $\text{Ru}^{\text{II}}$  complexes refers to these types of complexes). They are studied in a wide variety of fields; for photosensitization in solar energy conversion,<sup>20-28</sup> as probes and selective sensors of small molecules,<sup>29, 30</sup> in photo-catalysis,<sup>31-36</sup> for photo-chemotherapy,<sup>37, 38</sup> as building blocks in supra-molecular constructs,<sup>16, 39-43</sup> and in molecular electronics.<sup>41, 44, 45</sup>

When introducing  $\text{Ru}^{\text{II}}$  complexes in a photophysical or photochemical context, it is convenient to start off with the archetypical polypyridyl complex  $[\text{Ru}(\text{bpy})_3]^{2+}$ . This octahedral complex displays a prominent, broad metal-to-ligand charge transfer (MLCT) absorption band centered at  $\sim 450$  nm ( $\epsilon \sim 1.4 \times 10^4 \text{ M}^{-1} \text{ cm}^{-1}$ ).<sup>18</sup> Upon excitation, an electron is transferred from the metal

<sup>a</sup> A chromophore [color-lover (from Greek)] is the part of the molecule that is responsible for a given spectral band in the absorption spectra.

center to one of the ligands, formally yielding  $[\text{Ru}^{\text{III}}(\text{bpy})_2(\text{bpy}^-)]^{2+*}$ . Subsequent to excitation, the complex rapidly goes through intersystem crossing to form a triplet state ( $^3\text{MLCT}$ ),<sup>b</sup> emitting with a ca 1  $\mu\text{s}$  lifetime (at room temperature in acetonitrile).<sup>18</sup> This long lived  $^3\text{MLCT}$  state can in turn act as an energy donor, or electron donor or acceptor, with reversible redox chemistry in both the ground and excited state.<sup>16, 18, 19</sup>

Taking the bpy-ligand as a framework to build upon, substitution to the ligand backbone is a conventional strategy to shift energy levels in the complex to fine-tune redox potentials, absorption spectra and photoluminescence properties.<sup>15, 18, 46-48</sup> It is, in general, straightforward to do so by attaching electron withdrawing or donating groups. Extending the ligand with additional conjugated cycles is also common, with phen (phen = 1,10-phenanthroline)<sup>49</sup> and tpy (tpy = 2,2':6',2''-terpyridine)<sup>38, 41, 42, 45, 50, 51</sup> likely being the most studied tricyclic bi- and tridentate ligands respectively. Compared to bpy-substitutions, chelation of non-bpy type ligands, that are more bulky, or form additional coordination bonds, much larger differences can be observed in geometrical structure (such as bond lengths and angles), electrochemical and photophysical properties.<sup>52-54</sup>

Many of the applications mentioned earlier utilize specific functions, such as the anchoring group, which is used to attach complexes to a metal-oxide surface. This is commonly used for surface sensitization purposes, as in the dye-sensitized solar cell (DSSC)<sup>20, 21, 24</sup>, where the anchoring enables the electron (or energy) donor to be in close proximity to the acceptor. As energy and electron transfer rates depend exponentially on distances,<sup>55</sup> proximity is typically important for high efficiency. By attaching the electron donor and acceptor, the process can be several orders of magnitude faster than if in solution, where it is hampered by diffusion. The anchoring effectively allows the use of molecules with shorter lived excited states. While a general anchoring group can seem simple, determining the anchoring group's character and effect on electron transfer efficiency is a research sub-field of its own.<sup>56, 57</sup> In the specific case of DSSCs, some of the most efficient cells employ the Ru-dye called N3 or derivatives thereof.<sup>22</sup>

Another field where  $\text{Ru}^{\text{II}}$  complexes are common, related to the fossil fuel predicament, is in photocatalysis for solar fuel generation. This photocatalysis can be realized by water splitting for hydrogen evolution,<sup>33-35, 58-61</sup> or by carbon dioxide reduction into fuels like methanol.<sup>62-64</sup> The many accessible oxidation states of transition metal complexes makes them possible candidates as molecular catalysts for such energy demanding reactions. Here, as well as for DSSCs, there must be enough of a driving force for the reaction to occur, or the absorbed light will be wasted. On the contrary, having a too large overpotential to drive the reaction lowers the maximum photon-to-light energy efficiency, as large portions of the energy is dissipated as heat. While high enough energy photons can be used to activate a catalyst to drive the reaction in a brute force manner, a system relying on direct solar UV-radiation cannot achieve high overall photon conversion efficiency.<sup>65</sup> In these demanding reactions, the ligand and complex structures can aid the reaction by stabilizing intermediates via mechanisms such as

---

<sup>b</sup> This lowest excited state behaves as a single  $^3\text{MLCT}$  state, but is in fact comprised of several degenerate energy levels, even at liquid nitrogen temperatures, which have a mixed singlet-triplet character.

intramolecular hydrogen-bonding, and by utilizing the available oxidation states of the metal center. While my research interests are more towards photophysics and photochemistry, it should be mentioned that Ru<sup>II</sup> complexes also are common in (non-photo) catalysis.<sup>66-69</sup>

One effect of the octahedral geometry in a complex upon chelation to several different or to unsymmetric ligands, is the many possible isomers that can be formed (from the same set of ligands). This variety enables stereoselective and enantioselective catalysis schemes<sup>70</sup> by the complexes, as well as for possible use in supramolecular constructs.<sup>16, 42</sup> Another sort of isomerism is exhibited with chelated ambidentate ligands,<sup>71, 72</sup> such as sulfoxides, where Ru<sup>II</sup> preferably coordinates to sulfur and Ru<sup>III</sup> favors oxygen coordination.<sup>73-77</sup> This has led to the development of electrochromic complexes, where the removal of an electron from Ru<sup>II</sup> causes an isomerization which in turn yields a color change of the complex. Due to the MLCT nature of the visible Ru<sup>II</sup> absorption band, some of these complexes also exhibit photoisomerization, and are consequently photochromic.<sup>44, 74, 77, 78</sup> Apart from shifted absorption spectra, the complexes also exhibit large changes in other properties, such as oxidation potential, and these complexes have been proposed for use in molecular logic applications.<sup>41, 44</sup>

Other elaborate structures have been designed for highly specific sensing of small molecules, such as cyanide<sup>30</sup> or intracellular thiols.<sup>29</sup> The detection is enabled as the reaction with the target molecule drastically alters the photoluminescence, which typically is more sensitive to structural and environmental changes than absorption. Complexes with environmentally sensitive ligand structures, that report on the immediate surroundings of the complexes, as pH<sup>79</sup> or oxygenation,<sup>80</sup> have also been examined, again detectable by changes in the photoluminescence. Additionally, Ru<sup>II</sup> complexes with planar ligands can enantioselectively intercalate into DNA, utilizing the difference in polarity in the bulk and the DNA-helix.<sup>81</sup> DNA intercalating complexes have been proposed as anti-cancer drugs in photochemotherapy. By introducing bulky groups to put strain on the complex, resulting in distorted geometry, a complex can become more prone to photo induced ligand loss,<sup>38</sup> where the ejected ligand can react with DNA and irreversibly damage it, killing the malignant cell.<sup>37</sup>

The abovementioned applications utilize different aspects of the structural, photophysical, photochemical and electrochemical properties of Ru<sup>II</sup> complexes, depending on what task the complex is to perform. Their uses all rely on the ruthenium-ligand interactions and highlight the versatility of Ru<sup>II</sup> complexes. The structure of the ligands, their  $\sigma$ -donation and  $\pi$ -backbonding capabilities, and the way in which they are coordinated to the Ru-center determine the properties and function of the complex. Therefore, in a purposeful design of metal-complexes, it becomes necessary to understand structure-function relationships; how the electronic and geometric structure of the ligands affects the structure and properties of the complex. This structure-function relationship and its consequences for photophysical and photochemical properties is the focus of my thesis. Special attention will be given to heterocyclic, polydentate non-polypyridyl ligands, which I choose to call unconventional.



## 2. Background

### 2.1. Photophysics and Photochemistry

Photophysics describe how molecules absorb light and how the excited state evolves through radiative and non-radiative processes, not involving chemical change.<sup>17</sup> Photochemistry can be seen as an extension to photophysics, and takes off when the photoexcitation results in chemical reactions;<sup>17</sup> such as breaking or making of chemical bonds, or interactions between molecules, like electron transfer or photoinduced reactions.

#### 2.1.1. Light-matter interactions

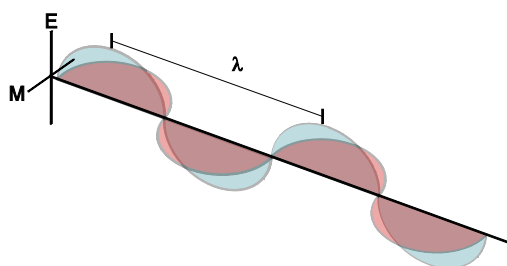
##### 2.1.1.1. Light

Light is the part of the electromagnetic spectrum covering ultraviolet, visible and infrared wavelengths (UV-Vis-NIR), coinciding with the most intense spectral features from the Sun, and roughly the part of the spectrum we can see. The energy ( $E$ , joule), frequency ( $f$ ,  $s^{-1}$ ), speed ( $c$ ,  $\sim 3 \times 10^8 \text{ ms}^{-1}$ ) and wavelength ( $\lambda$ ,  $m^{-1}$ ) of light are related as:

$$E = hf = hc/\lambda \quad 1$$

Where  $h$  is Planck's constant ( $6.626 \times 10^{-34} \text{ J s}$ ), which is deeply connected with quantum mechanics. The constant arose in connection to the theory of quantization of light, resulting in the light particle, the photon.

The electromagnetic wave consists of three vectors: A propagation vector, an electric field vector, and a magnetic field vector, where the electric and magnetic fields are orthogonal to both each other and the propagation vector, Scheme 2.



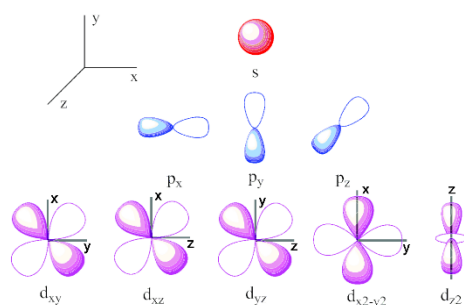
**Scheme 2.** Illustration of electromagnetic wave with electric (blue) and magnetic (red) field vectors perpendicular to the propagation direction (black line).

When the orientation of the electric field vectors of a light beam line up, the light is polarized. From most light sources, the orientation is randomized, and the light is non-polarized. The wave nature of light also results in possible interference effects. Constructive and destructive interference result from the addition of electric field vectors, yield higher or lower intensity of the light respectively, and depend on the wavelength, coherence and phase of the wave. For two waves that are out of phase by  $\lambda/2$  but otherwise identical, the sum of their electric vectors cancels out, and the intensity is zero. When they are in phase, the resulting electric field is twice that of a single wave.

### 2.1.1.2. Matter

Protons, neutrons and electrons are the smallest constituents of matter which this thesis, and chemistry in general, is concerned about. Any given atom has a core of neutrons and protons, and electrons in orbits around the nucleus, balancing the positive charge of the protons. The atomic orbitals (AOs) are in essence the solutions to the *Schrödinger equation* for the system, but due to the immense complexity of many-electron systems, the only analytical solutions are that for one electron systems (H, He<sup>+</sup>, Li<sup>2+</sup> ...).<sup>82</sup> As a result, a number of assumptions and simplifications have been developed. One of the more important assumptions is the *Born-Oppenheimer approximation*, which states that nuclear, spin and electron motions can be decoupled, due to their different time dependence, as electrons are much lighter than the nucleus they move much faster.<sup>83</sup> The population of different AO's is governed by the *Aufbau* and *Pauli exclusion principles*; which state that the lowest energy orbitals are occupied first, followed by higher energy orbitals, and that no orbital can be occupied by more than two electrons with opposite spins.<sup>83, 84</sup>

These orbitals are 3-dimensional representations of the probability density of where an electron can be found, should the orbital be occupied. The atomic orbitals *s*, *p*, and *d* are depicted in Scheme 3. For molecules, the molecular orbitals (MOs) can be constructed through linear combinations of AOs, leading to hybrid orbitals.<sup>83, 85</sup> Following the *Pauli exclusion-* and *Aufbau principles*, the electronic structure of the molecule can be generated.



**Scheme 3.** Atomic orbitals, *s*, *p* and *d*.

Taking formaldehyde, H<sub>2</sub>CO, as an example, the combination of AOs into MOs result in the electronic configuration ( $\psi$ ), in order of increasing energy:

$$\psi = (1s_o)^2(1s_c)^2(2s_o)^2(\sigma_{CH})^2(\sigma'_{CH})^2(\sigma_{CO})^2(\pi_{CO})^2(n_o)^2(\pi_{CO}^*)^0 \quad 2$$

Which AOs the MOs are generated from is indicated by the subscripts, and the superscript indicate the occupancy (number of electrons), where  $\sigma$  and  $\pi$  are shared by more than one atom. The highest occupied molecular orbital (HOMO) is thus the non-bonding  $(n_o)^2$ , and the lowest unoccupied molecular orbital (LUMO) is the anti-bonding  $(\pi_{CO}^*)^0$ . Larger molecules have myriads of orbitals, and the expressions for the electronic configurations are usually abbreviated, and for formaldehyde it becomes:

$$\psi = K(\pi_{CO})^2(n_o)^2 \quad 3$$

Which is the ground state configuration, and where  $K$  denotes the closely bound electrons from the terms in Equation 2.

### 2.1.1.3. Interaction

Electromagnetic radiation can perturb a molecule, inducing a transition between two states. For electronic transitions to occur, as the promotion of an electron from a lower to a higher energy orbital, photon energies in the UV-Vis-NIR regime are commonly required. Photon energies that are much higher or lower than that of light correspond to different molecular or nuclear transitions. Different wavelength regimes are used in spectroscopic techniques to study nuclear magnetic resonances (NMR, radio waves), vibrational transitions (infrared), and crystal structures (X-rays). While all these spectroscopic methods are represented in the appended publications, my work focus on discerning the electronic transitions, by means of optical spectroscopy and electrochemistry.

For electronic transitions to occur, such as promoting an electron from LUMO to HOMO by the absorption of light, the two states must be coupled, *i.e.* the wave functions must share an overlap. A larger coupling element is consistent with a higher probability of the transition to occur, which for instance can be observed as a more prominent absorption in optical spectroscopy. This can be expressed as the *Golden rule*:<sup>83</sup>

$$k = \frac{2\pi}{\hbar} \rho \langle \psi_1 | H | \psi_2 \rangle^2 \quad 4$$

Where  $k$  is the rate of exchange between the two states,  $\rho$  is the density of states that couple to the initial state (the degeneracy),  $\hbar$  is Planck's constant divided by  $2\pi$ , and the last term is the matrix element coupling the perturbation ( $H$ ) of the final ( $\psi_2$ ) and initial ( $\psi_1$ ) states. Without taking a deep dive into quantum mechanical operators, the *Golden rule* can be related to the probability of a transition to occur based on the similarities between the initial and final states while taking into account the perturbing force,  $H$ . For light induced transitions, the electric field vector (the perturbation) must also be of appropriate alignment for the light to be absorbed.<sup>86</sup> As the absorption of light is dependent on the orientation of the electromagnetic field in relation to the transition dipole moment of the molecule, the polarization is important to take into account in emission experiments and in samples where the molecules are not randomly distributed.<sup>c</sup>

Certain transitions are not quantum mechanically allowed, such as the transitions between singlet and triplet states. This transition requires a spin-flip to occur, so called intersystem crossing, which is spin-forbidden by the first order assumptions made so far. By introducing spin-orbit coupling, a component mixing the spin angular momentum and the orbital angular momentum of the electron, the total momentum can be preserved during the spin-flip.<sup>83</sup>

Transitions are symmetric with respect to direction, which means absorption and emission rates both depend on the extent of coupling between the two states involved in the transition.<sup>83</sup> In

---

<sup>c</sup> The effect of polarization upon absorption and emission is known as anisotropy, but is not included in my work or in this thesis, apart from avoiding anisotropic effects.

fact, light induced absorption and emission (known as stimulated emission) are equally likely upon perturbing the molecule by light of the corresponding wavelength. This symmetry provides the fundamental mechanism for lasers (*light amplification by stimulated emission radiation*), which relies on molecular systems where the upper energy level is populated to a greater degree than the lower one.<sup>84</sup>

#### 2.1.1.4. In the hot spot

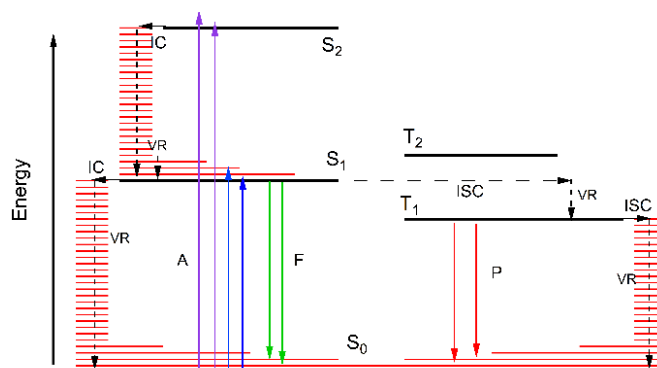
At ambient temperatures, most molecules are in the ground state (GS), as the available energy of the surroundings is not high enough to vibrationally excite the molecule. The Boltzmann distribution describes the ratio of an upper and a lower energy level:

$$\frac{N_2}{N_1} = \frac{g_2}{g_1} e^{\frac{E_2 - E_1}{k_B T}} \quad 5$$

Where  $N_i$  is the number of molecules occupying the state of energy  $E_i$ ,  $k_B$  is Boltzmann's constant ( $\sim 1.38 \times 10^{-23}$  J/K or  $\sim 8.62 \times 10^{-5}$  eV/K) and  $g$  denotes the degeneracy of the energy level at temperature  $T$ . This relation can be used to envision just how much energy visible photons carry. To equally populate an electronic upper and lower state of a blue absorbing molecule, corresponding to 2.75 eV (450 nm), the local temperature would have to be as high as 32 000 K. As chemical reactions proceed faster with increasing temperature (or more correctly, with increasing excess energy), subsequent to absorption of light, molecules are much more reactive.

### 2.1.2. Photophysical processes

An overview of possible transitions can be seen in the *Jablonski diagram*,<sup>86, 87</sup> Scheme 4.



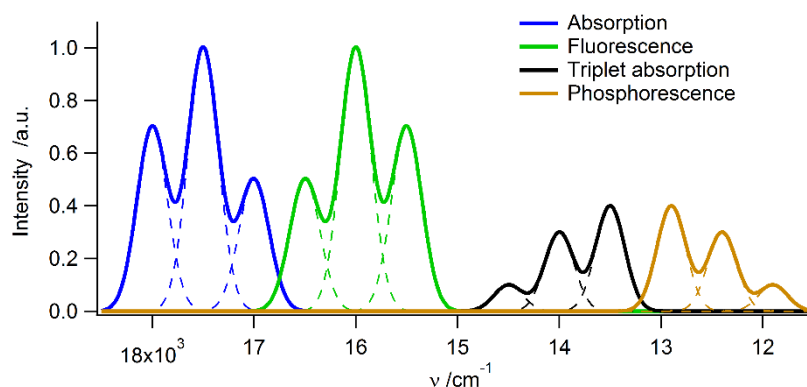
**Scheme 4.** Jablonski diagram depicting the electronic levels (bold black lines), vibrational levels (red lines) and electronic transitions in a molecule.  $S_x$  and  $T_x$  are singlet and triplet states respectively, A is absorption, F is fluorescence, P is phosphorescence, VR is vibrational relaxation, IC is internal conversion, ISC is intersystem crossing, and Q is quenching. Solid and dashed lines denote radiative (vertical) and non-radiative processes respectively.

All photonic transitions, *i.e.* those involving light, occur vertically in the diagram, and it imply that no nuclear rearrangement occurs on the timescale of the transition.<sup>d,88</sup> These so called

<sup>d</sup> Absorption proceed on the order of attoseconds (as), and beyond the time resolution of most equipment. Laser spectroscopists have started to elucidate the absorption process with elaborately synthesized as-pulses.

*vertical transitions* are a consequence of the *Franck-Condon principle* (electronic transitions occur much faster than the nuclei can respond), which in turn is a consequence of the *Born-Oppenheimer approximation* (electronic and nuclear wave functions can be separated).

The lowest energy configuration of a molecule is in the vast majority of cases a singlet state,  $S_0$ , and light induced electronic transition (absorption) originates from this state. The spin-allowed transition from  $S_0$  to higher, excited states are to  $S_1$ ,  $S_2$ ,  $S_3$  and so forth. In general, internal conversion (IC) and dissipation of energy as heat via vibrational relaxation (VR) rapidly takes the higher excited states to the vibrationally relaxed  $S_1$  state. This state can go through radiative decay by photon emission (fluorescence, F), or via non-radiative pathways, by IC to  $S_0$  or intersystem crossing (ISC) to a triplet state, such as  $T_1$ . As we saw in the previous section, the rate of intersystem crossing is highly dependent on the possibility for spin-orbit coupling, which in general increases with increasing atom weight, known as the *heavy atom effect*.<sup>83, 89, 90</sup> In fact, molecules with heavy atoms can exhibit intersystem crossing rates far exceeding those of other decay paths from the  $S_1$  state.  $T_1$  in turn can go through ISC or spin-forbidden emission of a photon (phosphorescence) to end up back in  $S_0$ . In the vast majority of cases, emission from a molecule proceeds by the transition from the lowest accessible state of any given multiplicity, such as  $S_1$  or  $T_1$ , to the ground state; an observation known as *Kasha's rule*.<sup>86, 91</sup>



**Scheme 5.** Illustration of transitions involving light: The absorption, fluorescence, triplet absorption and phosphorescence (solid) and vibrational transitions contributions (dashed) of an imaginary molecule, as constructed from a series of Gaussians.

The  $S_0$ - $S_1$  transition likely ends up in the vibrationally excited (or hot)  $S_1$ , and the  $S_1$ - $S_0$  transition likely result in a hot  $S_0$ . This lead to an anti-symmetry in the absorption and emission spectra, known as the *mirror image rule*, Scheme 5.<sup>86</sup> The resulting energy difference between the absorption and emission is known as the Stokes-shift,<sup>e,86</sup> which is related to the vibrational energy spacing. The absorption and emission symmetry is also seen in the absorption strength and in the rate constant of emission, both relying on the overlap integral between the states. However, while phosphorescence is readily observed for many samples, triplet absorption ( $S_0$ - $T_x$ ) is in general very weak, and thus not observed.

<sup>e</sup> Raman scattering, with Stokes and anti-Stokes shifts, is related and shares the energy shift, but proceeds via different processes.

Experimental chemists usually give the strength of the absorption for molecules in molar absorptivity ( $\epsilon$ ,  $M^{-1}cm^{-1}$ ). This parameter,  $\epsilon$ , is included in the *Lambert-Beer's law of absorption*:

$$A(\lambda) = \log\left(\frac{I_0(\lambda)}{I(\lambda)}\right) = bC\epsilon(\lambda) \quad 6$$

Where the absorption ( $A$ ), is proportional to the logarithmic ratio between incident ( $I_0$ ) and outgoing light ( $I$ ), depending on wavelength ( $\lambda$ ). On the right hand side is the path length of the sample container ( $b$ ), and the concentration ( $C$ ) of the molecule. For samples with different molecules, *Lambert-Beer's law* describes the total absorption as a linear combination of the individual contributions.

### 2.1.3. Photochemical reactions

While photophysical events keep the molecule intact, photochemical reactions alter the molecule. A few common photochemical reactions for the excited molecule ( $M^*$ ) are:



For bimolecular reactions, the rate of collision, and subsequent reactions are dependent on the concentration and diffusion of the molecules as well as the excited state lifetime.

The excitation energy can also result in the decomposition of the molecule. As an example, the excess energy can cause a metal complex ( $ML_x$ ) to eject a ligand ( $L$ ), which opens a coordination site for further reactions:



In several cyclic processes, no net chemistry is attained, such as in photocatalysis or dye sensitization schemes. The excess energy of the excited molecule is utilized to either drive a current via electron transfer, as in DSSCs,<sup>20</sup> or to store the energy in chemical bonds, as in photocatalysis.<sup>31</sup> While the molecule experiences transient modifications, the initial state is regenerated via additional reactions. These kind of cyclic reactions are of major importance in the fields related to solar energy conversion.<sup>20, 92, 93</sup>

### 2.1.4. Quantum yields and rates of photoinduced processes

Consecutive to absorption, the excited state decay depends on all accessible pathways and their corresponding rate constants. The quantum yield ( $\Phi$ ) of any given process is defined as the number of events per absorbed photons, and ranges from 0 to 1 (for 1-photon-1-event

processes).<sup>f</sup> The lifetime of the excited state ( $\tau$ ), is inversely proportional to the sum of all rate constants ( $k_i$ ) of the deactivating processes. These parameters are described by:<sup>86</sup>

$$\Phi_{Em} = \frac{k_{rad}}{\sum_i k_i} \quad 12$$

$$\tau = \frac{1}{\sum_i k_i} \quad 13$$

The rate constants are commonly divided into two categories, radiative ( $k_{rad}$ ) and non-radiative ( $k_{nr}$ ).  $k_{nr}$  includes all processes not involved in the emission of photons, such as internal conversion, intersystem crossing, and quenching. The radiative rate constant depends on the internal structure of the molecule, and can for all practical purposes be considered temperature independent. On the contrary, the non-radiative deactivation of the excited state is highly dependent on temperature, as it involves both thermally activated intramolecular deactivation and collisional dissipation of the excitation energy. The radiative and non-radiative rate constants can be calculated from:<sup>86</sup>

$$k_{rad} = \frac{\Phi_{Em}}{\tau} \quad 14$$

$$k_{nr} = \frac{1 - \Phi_{Em}}{\tau} \quad 15$$

Quenching of the excited state via bimolecular processes, such as EnT and ET, depends on the concentration of the quencher, the quenching rate constant and the excited state lifetime. Triplet excited states usually display slower radiative decay than singlet excited states, due to the spin forbidden transition.<sup>83, 86</sup> As oxygen in the ground state is a triplet, it can quench triplet states by forming two singlet states (the quenched and the quencher molecule); in this process, highly reactive singlet oxygen is produced. Hence, the excited state lifetime, as well as photostability, can be substantially increased for many triplet emitters by de-aerating the sample solution. Additionally, the presence of oxygen can promote triplet formation from singlets.<sup>90</sup>

Another photochemical reaction is photoinduced isomerization, displayed by molecules such as azobenzenes, spiropyrans, and several transition metal complexes with ambidentate ligands (ambidentate ligands can coordinate in more than one way).<sup>94, 95</sup> In the case the photoisomerization is reversible, and can be driven in both directions by light, the distribution of isomers A and B when irradiated will depend on the product of the quantum yield of isomerization and the molar absorptivities as:

$$PSD(\lambda) = \frac{[A]_{\lambda,t \rightarrow \infty}}{[B]_{\lambda,t \rightarrow \infty}} = \frac{\Phi_{B \rightarrow A}(\lambda) \times \epsilon_B(\lambda)}{\Phi_{A \rightarrow B}(\lambda) \times \epsilon_A(\lambda)} \quad 16$$

Where *PSD* is the *photostationary distribution* of isomers under continuous irradiation by light

<sup>f</sup> In cases where several photons are required for one event to occur, the quantum yield is theoretically limited to  $1/n$  where  $n$  is the number of photons required. When several events can proceed from a single excitation, the theoretical maximum quantum yield becomes  $n/1$ , where  $n$  is number of events per excitation.

with wavelength  $\lambda$ ,  $\Phi$  is the quantum yield of isomerization in the respective direction. As  $\epsilon$  for A and B differs, the concentration distribution will depend on irradiation wavelength.

### 2.1.5. Non-linear optical effects.

All the photophysical processes so far have been concerned with single photon interactions, while stringently the interaction is described by a power series of the optical susceptibility,  $\chi$ :<sup>84</sup>

$$\mathbf{P} = \epsilon_0(\chi_1\mathbf{E} + \chi_2\mathbf{E}^2 + \chi_3\mathbf{E}^3 + \dots) \quad 17$$

Where  $\mathbf{P}$  is the polarization vector,  $\mathbf{E}$  is the electric field strength, and  $\epsilon_0$  is the permittivity of vacuum. As the multi photon interactions depend exponentially on the light intensity per area ( $\text{W m}^{-2}$ ), these effects are commonly too small to be of significance in most experiments. However, short laser pulses can provide extremely high peak effects. For instance, a  $10 \text{ mm}^2$ , 100 fs pulse of 1 mJ would peak at  $10^{15} \text{ W m}^{-2}$ ; in comparison, the solar radiation we receive on an ordinary day is on the order  $10^3 \text{ W m}^{-2}$ , if we are lucky.

The interaction of light with the second term in Equation 17,  $\chi_2$ , can be utilized to achieve doubling of the light frequency, the so called second harmonic generation (SHG). Third (THG) and higher order harmonic generation can also be performed, and in this way a 1000 nm laser can provide 500, 333, 250, ... nm light as well; however with diminishing returns.<sup>84</sup>

## 2.2. Electron Transfer

There is a strong connection between photophysical, photochemical and electrochemical properties,<sup>96</sup> which are all coupled to the electronic structure of the molecule. In electrochemistry, for transition metal complexes, the lowest energy oxidation (removal of the first electron) is expected to occur from the HOMO, while the lowest energy reduction (addition of the first electron) is to the LUMO.<sup>18</sup>

Spontaneous electron transfer requires a driving force to occur, which arises as the reduction and oxidation potentials of two species differs. The half-cell reactions can be contemplated to find suitable electron transfer pairs of electron donors ( $D/D^+$ ) and electron acceptors ( $A/A^-$ ). While the process is in principle the same for ground state and excited state molecules, the excited state reactivity is usually greatly enhanced due to the excess energy corresponding to  $E_{00}$ , as seen in the equation for *Gibbs free energy of photo induced electron transfer*:<sup>17</sup>

$$\Delta G^0 = e \left[ E^0 \left( \frac{D^{+\bullet}}{D} \right) - E^0 \left( \frac{A}{A^{-\bullet}} \right) \right] + \frac{z(D^{+\bullet})z(A^{-\bullet})e^2}{4\pi\epsilon_0\epsilon_r r} - \frac{z(D)z(A)e^2}{4\pi\epsilon_0\epsilon_r r} - E_{00} \quad 18$$

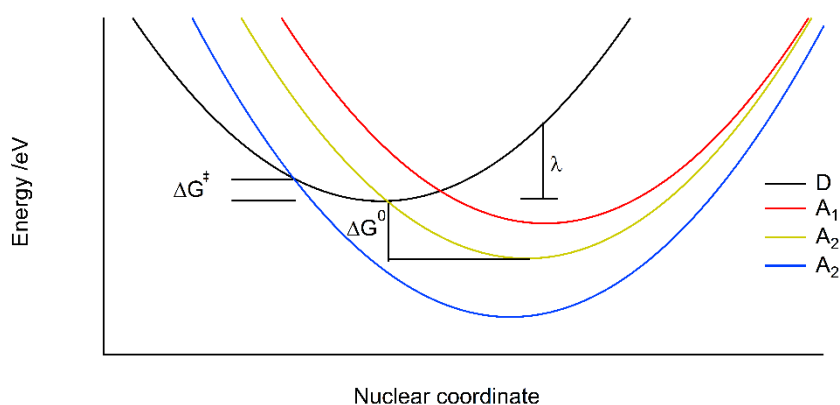
Where  $\Delta G^0$  is the free energy of the reaction,  $E^0$  is the energy of the corresponding half-reactions,  $z$  is the charge,  $\epsilon_0$  and  $\epsilon_r$  is the permittivity of vacuum and the relative permittivity of the solvent, and  $r$  is the distance between A and D after the reaction.  $E_{00}$  is, as previously described, the difference between the vibrationally relaxed GS and ES.

The modern theory of electron transfer was first proposed by Marcus in 1956<sup>97</sup>, and is simply called Marcus theory (of electron transfer), although others, like Hush, Closs and Miller also

have made major contributions to develop and prove the theory.<sup>98,99</sup> In Marcus-theory, the rate of electron transfer,  $k_{ET}$ , for weakly coupled donor-acceptors is described by:<sup>96</sup>

$$k_{ET} = \sqrt{\frac{4\pi^3}{h^2\lambda k_B T}} V_{DA}^2 \times e^{\frac{-(\Delta G^0 + \lambda)^2}{4\lambda k_B T}} \quad 19$$

Where  $\lambda$  is the reorganization energy, and  $V_{DA}$  is the electronic coupling between the two states. The parameters in the exponent can be interpreted from the potential energy surface diagram, Scheme 6. In these diagrams, the energy of the different states are plotted versus a reaction coordinate, for instance the distance between the donor and acceptor.



**Scheme 6.** Illustration of energy parabolas for an electron donor (D) and three electron acceptors (A). The free energy of reaction ( $\Delta G^0$ ), reorganization energy ( $\lambda$ ) and free energy of activation ( $\Delta G^\ddagger$ , see Equation 20 below) are marked in the figure. The three acceptor parabolas are chosen so that 1)  $\Delta G^0 < \lambda$ ,  $\Delta G^0 = \lambda$ , 2)  $\Delta G^\ddagger = 0$ , and 3)  $\Delta G^0 > \lambda$ . The couple D-A<sub>3</sub> is in the inverted region.

As the charge distribution in the molecule changes during the reaction, the solvent (outer components) and molecular bonds (inner components) rearranges, corresponding to the reorganization energy ( $\lambda = \lambda_{In} + \lambda_{Out}$ ). While  $\lambda_{In}$  is dependent on the reaction,  $\lambda_{Out}$  is dependent on the reaction as well as the solvent polarity.<sup>96</sup> Accounting for the reorganization energy, the free energy of activation,  $\Delta G^\ddagger$ , becomes:

$$\Delta G^\ddagger = \frac{(\Delta G^0 - \lambda)^2}{4\lambda k_B T} \propto -\ln(k_{ET}) \quad 20$$

The reorganization energy in ET can also be related to asymmetry in absorption and emission energies. As the correct nuclear coordinates must be adopted prior to vertical transitions, absorption by necessity requires more energy than is emitted subsequent to nuclear rearrangements.<sup>100</sup>

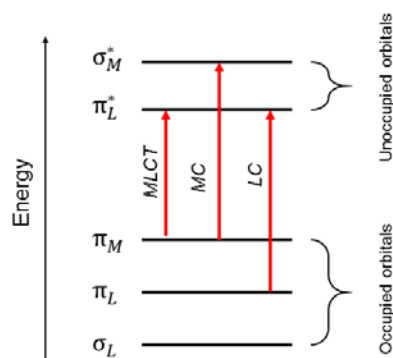
The Marcus theory predicts unintuitive effects when the driving force becomes increasingly negative,  $\Delta G^0 < -\lambda$ , resulting in a slower rate of electron transfer, as can be interpreted from Equation 20. The prediction of the *inverted region*, predated the experimental proof by ca 30 years,<sup>99</sup> and subsequent to this, Marcus was awarded with the Nobel Prize.

## 2.3. Ru<sup>II</sup> complexes

### 2.3.1. Electronic structure of archetypical Ru<sup>II</sup> complexes

The much studied ruthenium complex [Ru(bpy)<sub>3</sub>]<sup>2+</sup> display remarkably rich photophysical, photochemical and electrochemical properties. To understand how these properties arise one needs to look closer to the electronic structure of the complex, from where the properties originate.

The uncoordinated Ru-atom has 5 degenerate *d*-orbitals, but this degeneracy is broken upon chelation with the bpy-ligands, producing a octahedral complex, and the resulting energy levels are depicted in Scheme 7.<sup>85</sup>



**Scheme 7.** Illustration of energy levels in [Ru(bpy)<sub>3</sub>]<sup>2+</sup>. Subscript *M* and *L* are for metal and ligand associated orbitals, respectively. Transitions indicated by red arrows, ordered in energy difference from left to right.

The resulting Ru<sup>2+</sup> complex has a fairly large energy splitting between the filled and empty orbitals, with a high electron density being localized on the metal center in the HOMO ( $\pi_M$ ).<sup>16, 18, 19</sup> On the contrary, the LUMO ( $\pi_L^*$ ) is ligand localized, resulting in the HOMO–LUMO transition being a metal-to-ligand charge transfer (MLCT), Scheme 7. Subsequent to the MLCT transition, the complex has a formally reduced bpy and an oxidized Ru-center, [Ru<sup>III</sup>(bpy)<sub>2</sub>(bpy<sup>-</sup>)]<sup>\*2+</sup>.<sup>16, 18, 19</sup> This lowest energy transition has a broad absorption feature with fairly strong absorption in the blue region, centered at ca 450 nm, Figure 1.

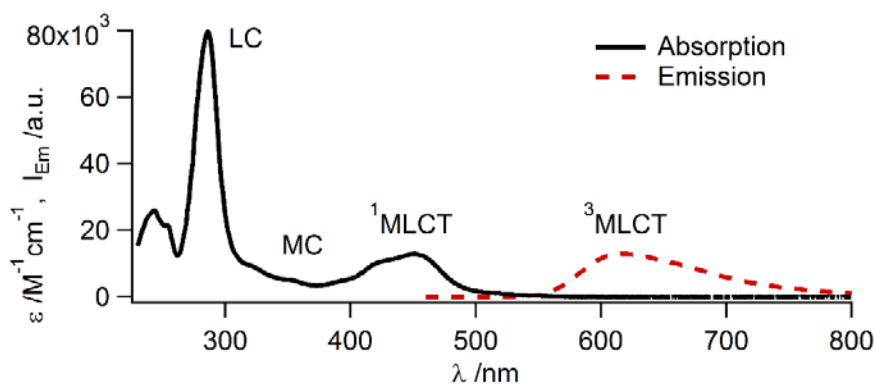
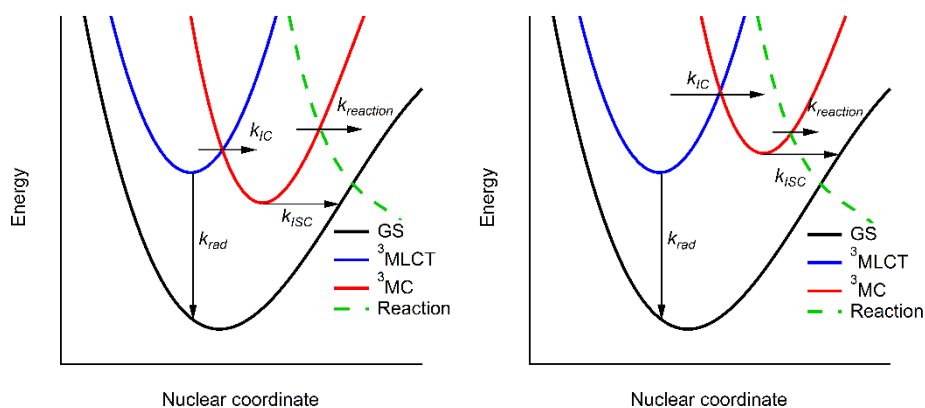


**Figure 1.** Absorption ( $\epsilon$ ) and emission spectra ( $I_{Em}$ ) of [Ru(bpy)<sub>3</sub>]<sup>2+</sup> in acetonitrile. Transitions from Scheme 7 indicated in figure.

The charge nature of the transition is coupled to a high transition dipole moment, attributed to the high molar absorptivity of the transition as compared to many other transition-metal transitions; however, this is still lower than the  $\pi-\pi^*$  transitions of many conjugated organic compounds, like the ligand-centered (LC) transition in bpy. Additional absorption features arise due to metal-centered (MC), and LC transitions, which do not involve a charge transfer by excitation.<sup>16, 18, 19</sup>

Upon excitation, the large spin-orbit coupling in the presence of the heavy Ru-atom induces a rapid (<50 fs) intersystem crossing,<sup>101</sup> followed by relaxation to the lowest excited triplet state ( $\sim 1$  ps, depending on solvent),<sup>102</sup> yielding a triplet MLCT state ( $^3\text{MLCT}$ ). The  $^3\text{MLCT}$  state can subsequently thermally populate the  $^3\text{MC}$  state, or decay to the GS via either radiative or non-radiative processes, Scheme 8.<sup>18, 19</sup> At lower temperatures, the Boltzmann distribution between the two forms can be suppressed by slowing down the kinetics of surface crossing, according to the Arrhenius equation for rate constants of activated processes. The  $^3\text{MC}$  state is non-emissive and commonly involved in photochemical reactions, specifically ligand loss reactions that can occur because of elongated coordination bonds (nuclear coordinate in Scheme 8).<sup>18, 103</sup>



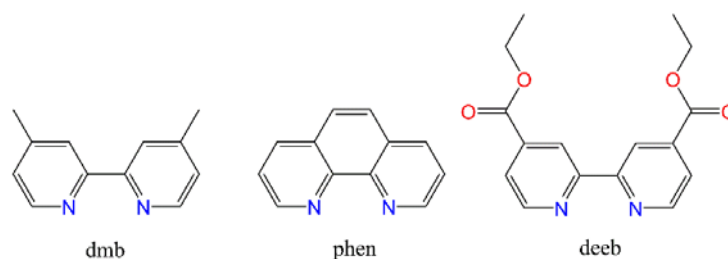
**Scheme 8.** Projected potential energy surfaces for the ground state (GS), triplet metal-to-ligand charge transfer ( $^3\text{MLCT}$ ) and triplet metal-centered ( $^3\text{MC}$ ) states of two  $\text{Ru}^{\text{II}}$  complexes. A small  $^3\text{MLCT}$ - $^3\text{MC}$  splitting and displacement in the left result in fast surface crossing ( $k_{\text{IC}}$ ), resulting in lower quantum yield of emission as  $k_{\text{rad}}$  is comparably small. Subsequent to surface crossing, intersystem crossing to the ground state ( $k_{\text{ISC}}$ ) or reaction ( $k_{\text{reaction}}$ , such as ligand loss). In the right picture, the uphill process in the right figure indicate a significantly slower population of the  $^3\text{MC}$  state. A larger displacement in the  $^3\text{MC}$  state suggests higher likelihood of ligand loss reactions.

The excited state lifetime, emission quantum yield and photostability of a  $\text{Ru}^{\text{II}}$  complex are thus strongly dependent on the energy difference and geometrical displacement between the  $^3\text{MLCT}$  and  $^3\text{MC}$  states.  $\text{Ru}^{\text{II}}$  complexes with a small  $^3\text{MLCT}$ - $^3\text{MC}$  energy difference, left side of Scheme 8, usually display fast deactivation of the excited state.<sup>18, 51, 103</sup> However, if the  $^3\text{MC}$  state is substantially distorted, the activation barrier can be high even if the process is isoenergetic, or even downhill.<sup>104</sup> In contrast to closely spaced  $^3\text{MLCT}$  and  $^3\text{MC}$  states, complexes displaying destabilized  $^3\text{MC}$  states, right side of Scheme 8, commonly have longer lived  $^3\text{MLCT}$  states displaying higher quantum yield of emission. Furthermore, for transition metal complexes in general, the *energy gap law* predicts that the excited state lifetime decreases

exponentially with the decrease in emission energy, *i.e.* the energy gap between the ES and GS.<sup>105, 106</sup>

### 2.3.2. Structural influences on the excited state manifold

By substitutions to the bpy-ligand with electron withdrawing or donating groups (EWGs or EDGs) the energy of the molecular orbitals can be changed.<sup>18, 46-48, 107</sup> Three ligands structurally similar to bpy are dmb (4,4'-dimethyl-2,2'-bipyridine), phen (1,10'-phenanthroline) and deeb (4,4'-diethyl ester-2,2'-bipyridine), Scheme 9. By withdrawing electron density from the  $\pi^*$ -system of the ligand, the MLCT state can be stabilized as the electron affinity increases; and vice versa for EDGs. In many cases, the effects can also be observed electrochemically as a change in the reduction potential ( $\text{Ru}^{2+/+}$ ), or spectroscopically as a blue- or red-shifted absorption. Consequently, *if* the complex exhibit MLCT emission, the emission spectrum should also be shifted. While the emission, according to *Kasha's rule*, originates from the lowest excited state, the EWG or EDG effect is in general easier to observe for emission compared to absorption, as the absorption spectrum is usually cluttered with several overlapping transitions.<sup>91, 96</sup> The photophysical and electrochemical properties of some common  $\text{Ru}^{\text{II}}$  complexes are summarized in Table 1 for comparisons.



**Scheme 9.** Ligand structure of dmb, phen and deeb.

Another effect of substituents is the size of the conjugated  $\pi$ -system; where the larger one can delocalize the charge over a larger volume upon MLCT transitions. The larger electron transfer route causes an increased transition dipole moment, in turn increasing the molar absorptivity, as the absorption is proportional to the square of the transition dipole moment. In addition, an extended  $\pi$ -system can also stabilize the  $^3\text{MLCT}$  state.<sup>54, 108, 109</sup>

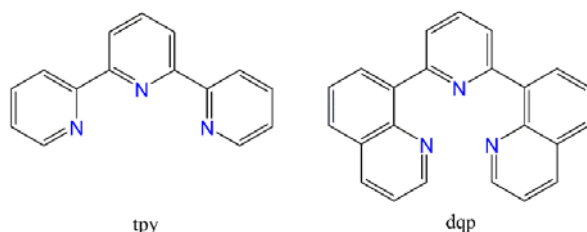
**Table 1.** Photophysical and electrochemical properties for several common  $\text{Ru}^{\text{II}}$  complexes. Oxidation ( $E_{\text{Ox}}$ ,  $\text{Ru}^{3+/2+}$ ) and reduction potential ( $E_{\text{Red}}$ ,  $\text{Ru}^{2+/+}$ ) versus  $\text{Fc}^{0/+}$  couple, wavelength of maximum absorption in visible region ( $\lambda_{\text{Abs}}$ ) and emission maximum ( $\lambda_{\text{Em}}$ ), in acetonitrile at ambient temperatures. All references from the extensive collection of Juris and coworkers,<sup>18</sup> unless otherwise noted.

Compound	$\lambda_{\text{Abs}}/\text{nm}$ ( $\epsilon / \text{M}^{-1}\text{cm}^{-1}$ )	$\lambda_{\text{Em}}/\text{nm}$ ( $\Phi, \tau / \mu\text{s}$ )	$E_{\text{Ox}}/\text{V}$	$E_{\text{Red}}/\text{V}$
$[\text{Ru}(\text{bpy})_3]^{2+}$	452 (13 000)	611 (0.059, 0.89)	+0.91	-1.71
$[\text{Ru}(\text{dmb})_3]^{2+}$	450 (17 000)	625 (0.041, 0.78)	+0.71	-1.84
$[\text{Ru}(\text{phen})_3]^{2+}$	442 (18 400)	604 (0.028, 0.46)	+1.02	1.79
$[\text{Ru}(\text{deeb})_3]^{2+}$	467 (22 700) <sup>110</sup>	626 (0.130, 2.10) <sup>110</sup>	+1.01	-1.34
$[\text{Ru}(\text{tpy})_2]^{2+}$	474 (14 600)	629 <sup>111</sup> ( $<10^{-5}$ , <sup>111</sup> $0.25 \times 10^{-3}$ )	+0.92 <sup>111</sup>	-1.67 <sup>111</sup>
$[\text{Ru}(\text{dqp})_2]^{2+}$ <sup>52</sup>	490 (14 000)	700 (0.02, 3.0)	+0.71	-1.70

The  $^3\text{MC}$  state can also be shifted by altering the ligand field strength, decreasing or increasing the splitting between the  $t_{2g}$  and  $e_g$  orbitals of the coordinated Ru-atom. This can be brought about by altering the coordination geometry, where a more octahedral complex destabilizes the  $e_g$  orbitals associated with  $^3\text{MC}$  states.<sup>85, 112</sup> Additionally, this energy splitting is also dependent on the  $\sigma$ - and  $\pi$ -bonding capabilities of the ligands, where good  $\pi$ -acceptors lower the  $^3\text{MLCT}$  associated  $t_{2g}$  orbitals, and strong  $\sigma$ -donors rise the energy of  $e_g$ .<sup>111, 113</sup> The adding/withdrawing of electron density to/from the metal center is also reflected by the  $\text{Ru}^{3+/2+}$  potential.

When coordinating phen, the ligand is more rigid than bpy-type ligands without the additional cycle, which forces the ligand to be more planar when chelated. The rigidity and planarity of the ligand will affect the Ru-N bond lengths as well as the bite-angles (N-Ru-N). In turn altering the energy of the  $^3\text{MC}$  and  $^3\text{MLCT}$  states respectively, and the energy splitting between these states.<sup>19, 53, 109</sup>

So far, mainly homoleptic – indicating that all ligands are the same – complexes with bidentate diimine (N,N) ligands have been discussed, with the principal composition  $[\text{Ru}(\text{N},\text{N})_3]^{2+}$ . Other motifs, like the tridentate (N,N,N), tpy (2,2':6',2''-terpyridine) or dqp (2,6-di(quinoline)pyridine), Scheme 10, can result in drastic change to the coordination geometry as well as ground and excited state properties. The two homoleptic complexes,  $[\text{Ru}(\text{tpy})_2]^{2+}$  and  $[\text{Ru}(\text{dqp})_2]^{2+}$  display more than 4 orders of magnitude difference in excited state lifetime, Table 1.<sup>52, 111</sup> The very short lifetime in  $[\text{Ru}(\text{tpy})_2]^{2+}$  has been ascribed to unfavorable bite angles and  $\sigma$ -donation, resulting in easily accessible  $^3\text{MC}$  states.<sup>50, 111</sup> Complexes with higher denticity, the number of coordination sites per ligand, usually exhibit less photoinduced ligand losses, simply due to the increased number of binding sites and possibility to re-coordinate.



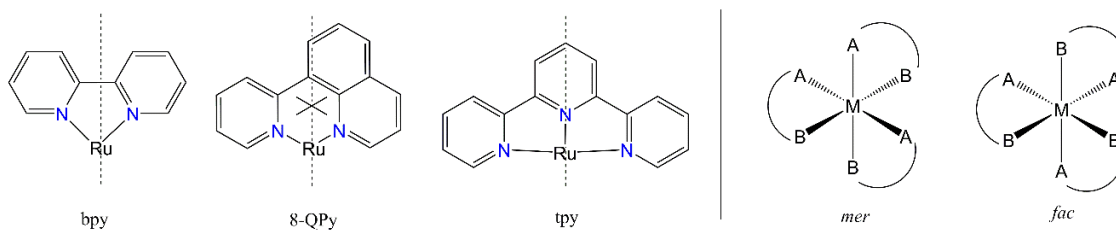
**Scheme 10.** Ligand structure of tpy and dqp.

### 2.3.3. Diastereomerism and induced isomerization

Coordinating symmetric bidentate ligands, A-A, to Ru results in homoleptic complexes with two isomers,  $\Delta$  and  $\Lambda$ , which are enantiomers (mirror images of one another). While the interaction with other chiral molecules or circularly polarized light differ between the two isomers, other differences in their physical properties are generally indistinguishable. With unsymmetric ligands like 8-QPy,<sup>8, 112</sup> with the general formula A-B, there are also the possibility of having the meridional (*mer*) or facial (*fac*) isomers, which have different *trans*- and *cis*-substituents, Scheme 11.

<sup>8</sup> 8-QPy is used to illustrate an unsymmetric ligand upon coordination, however, it is too sterically hindered to form homoleptic complexes.

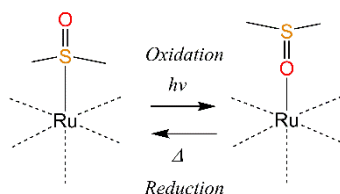
## 2. Background



**Scheme 11.** (Left) Symmetrical and unsymmetrical ligands when coordinated, with mirror planes (dotted). (Right) Illustration of *mer* and *fac* isomers.

For the *fac* isomer, all A are placed opposite to a B, while for the *mer* isomer the result is one of each of A-A, A-B, and B-B *trans*-coordination. Depending on the nature of the ligands, properties such as oxidation potential, absorption spectra and excited state lifetime can differ substantially between the *mer* and *fac* isomers, contrary to the enantiomers.<sup>114, 115</sup>

In the case with ambidentate ligands, a perturbation can lead to a rearrangement of the coordination sphere. This is observed for Ru-coordinated dimethyl-sulfoxide (dmsO), which can be either O- or S-chelated, and were the linkage-isomerization can be induced either by irradiation or electrochemically, Scheme 12.<sup>73, 75, 94, 116</sup>



**Scheme 12.** Photoinduced S-/O-isomerization in Ru-dmsO complex; forward reaction initiated by light, and thermal reversion.

The thermodynamically favored S-coordinated isomer is hence rearranged into the higher energy O-coordinated isomer. The O-coordinated state will reverse into the thermodynamically favored state given enough time.<sup>94</sup> However, if the reaction activation energy barrier is much higher than the available energy (*i.e.*  $\Delta E_a \gg k_B T$ ), the state can be kinetically trapped for extended periods of time, as seen for several polydentate ligands.<sup>77, 117</sup>

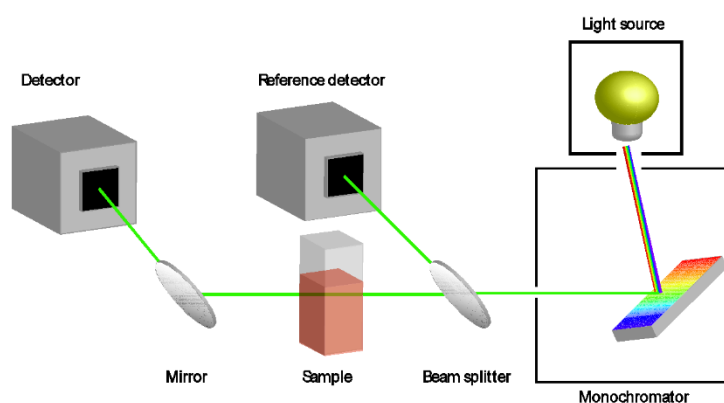
## 3. Methods and techniques

### 3.1. Absorption spectroscopy

In this thesis, three different electronic absorption spectroscopy techniques have been used, all in the UV-Vis-NIR region: 1) Steady-state absorption, 2) absorption-coupled photolysis, and 3) transient absorption.

#### 3.1.1. Steady state absorption spectroscopy

The experimental setup for steady state absorption measurements is presented in Scheme 13. The wavelengths of interest were selected by a monochromator from the spectrum of a broadband (white) light source. The intensity of the light before and after the sample were detected with photodiode detectors, whereby the spectra were recorded. Inherent solvent absorption was corrected by subtracting the baseline.



Scheme 13. Steady state absorption experimental setup.

#### 3.1.2. Absorption-coupled Photolysis

The spectral response to irradiation with time was followed by recording the absorption spectra, or single wavelengths, over time during continuous irradiation. The simultaneous irradiation and detection of absorption were carried out by introducing an additional light source perpendicular to the probe light in Scheme 13. The irradiation was provided by either narrow wavelength light sources as hand held lasers or LEDs, or a Xe-arc lamp with appropriately chosen filters.

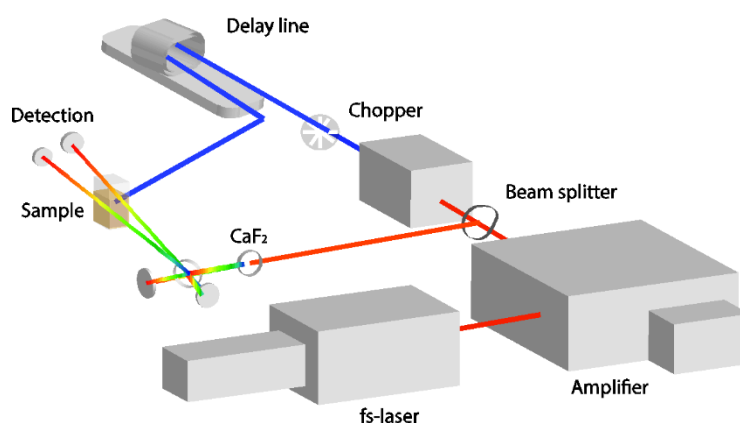
#### 3.1.3. Transient absorption spectroscopy

Transient absorption (TA) was performed to probe absorption of the excited sample, and record difference absorption spectra,  $\Delta A$ ; where the difference in absorption arises due to different molar absorptivities of the ground and excited states ( $\epsilon_{ES} \neq \epsilon_{GS}$ ). Positive features occur where  $\epsilon_{ES} > \epsilon_{GS}$  (excited state absorption) and negative features (ground state bleaching) are conversely appearing where  $\epsilon_{ES} < \epsilon_{GS}$ . By changing the time delay between the excitation (pump) and detection (probe) light, the time evolution of the excited state absorption was recorded.

Two different TA setups were used, based on the excited state of interest; 1)  $\sim 7$  ns fwhm pulse width, for ns-ms time regime, 2)  $\sim 100$  fs fwhm pulse width, for ps-ns excited state lifetimes.

The fs-TA setup is displayed in Scheme 14; the ns-TA setup was assembled in a similar fashion, but some of the components are not needed, see descriptions below.

The ns-TA setup consisted of a Nd:YAG laser (1064 nm, 7 ns fwhm, 10 Hz), and wavelengths for excitation were provided by second and third harmonic generation (SHG 532 nm, THG 355 nm). A tungsten lamp (250 W) provided the probe-light, and the transient signals were detected by either a CCD camera or a photo-multiplier tube (PMT). In both cases, the time resolution was achieved on the detection side, by electronic components. For detection with the PMT, monochromators were used before and after the sample to select probe wavelengths. CCD cameras can detect a full spectra at once, by diffracting the incoming light over a multi-channel detector array.



**Scheme 14.** Pump-probe experimental setup for transient absorption measurements.

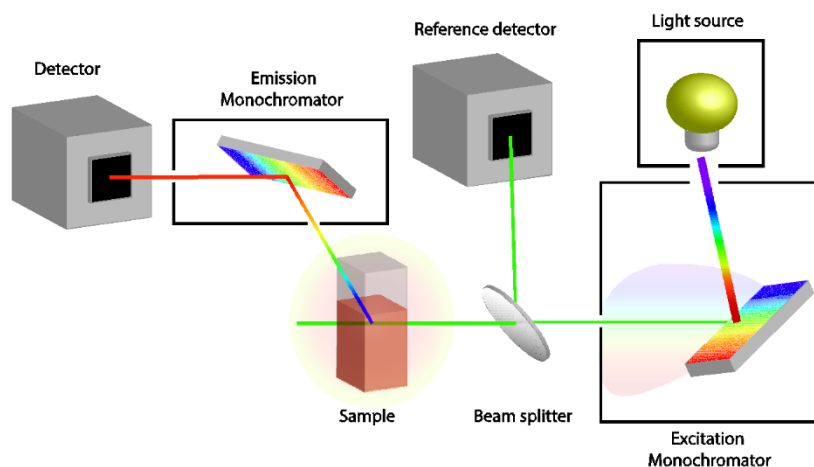
In the fs-TA setup, the initial pulses (120 fs, 800 nm, 82 MHz, 800 mW) were provided by pumping a Ti:Sapphire with a Millennia laser. This seed beam was amplified in a Spitfire pumped by an additional Nd:YLF laser (Evolution). The resulting beam (120 fs, 800 nm, 1 kHz, 800 mW) was split into two beams; one for producing the pump and one for the probe light. The pump beam was generated in an optical parametric oscillator (TOPAS), and subsequently lead through a chopper, as to allow measuring with and without the pulse. The timing between the pump and probe was controlled by changing the path length of the pump beam with a delay line. The probe light was generated in a CaF<sub>2</sub>-plate by white light generation, with a spectral distribution ranging from 800 nm down to ca 380 nm. The probe was further split into two beams, and directed through the sample, one that was overlapping with the pump and one that was not, into two optical fibers leading to a CCD camera. This resulted in a total of 4 spectra (pump on/off, pump present/absent), where the detection with the pump absent was used for correcting for pulse-to-pulse variations. Measurements were performed at the *magic angle* (54.7°) to avoid anisotropic effects.

## 3.2. Emission spectroscopy

### 3.2.1. Steady state emission spectroscopy.

Steady state emission spectra were recorded in a setup depicted in Scheme 15. The wavelength resolution was achieved by two monochromators. Collection of emission spectra was done by sweeping the emission monochromator, while excitation spectra were collected by scanning the

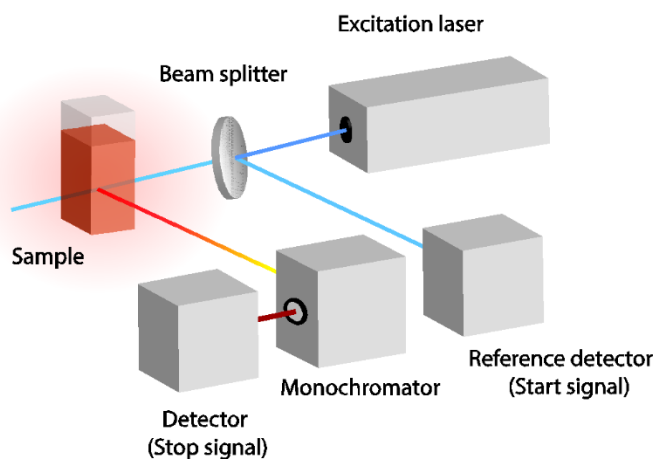
excitation monochromator. The excitation light was provided by a Xe-arc lamp and the detection was performed with a PMT. Correction for wavelength dependent detector response was performed.<sup>86</sup>



**Scheme 15.** Illustration of typical steady state emission spectroscopy setup.

### 3.2.2. Time resolved emission spectroscopy.

Time resolved emission was recorded using a time-correlated single photon counting (TC-SPC) setup, Scheme 16. As the name suggest, the TC-SPC setup detects a single photon at a time, and measure the time between the excitation pulse (start-signal) and the detected photon (stop-signal). For description of the electronic detection and signal converting system, see *e.g. Principles of fluorescence spectroscopy* by Lakowicz.<sup>86</sup>



**Scheme 16.** Simplified TC-SPC setup.

Excitation light was provided by high repetition rate pulsed diode lasers, and the emitted light was detected at right angle to the excitation light. To avoid over-counting,<sup>86</sup> the detection rate was always kept below 1% of the pulse repetition rate. Instrumental response functions were recorded at the excitation wavelength with a scattering solution.

### 3.3. Relative actinometry

Quantum yields ( $\Phi$ ) were estimated using relative actinometry by relating the recorded signal from the sample to a reference compound with known quantum yield. Both reference and sample were set to the same initial absorption.

#### 3.3.1. Emission quantum yields

For emission quantum yields, reference molecules were chosen to have similar absorption and emission spectra as the sample molecule, to minimize errors arising from the wavelength dependence of the apparatus. The quantum yield was calculated from:<sup>86</sup>

$$\Phi = \Phi_R \frac{\int_0^\infty I(v) dv}{\int_0^\infty I_R(v) dv} \frac{A_R n^2}{A n_R^2} \quad 21$$

Where the integrals are the integrated emission quanta,  $A$  the absorbances, and  $n$  the refractive indices for the sample and the reference. The indices of refraction are used to correct for the amount of light originating from a point source reaching the detector.<sup>h</sup>

#### 3.3.2. Quantum yield of photochemical reactions

Determination of photochemical quantum yields were calculated from:

$$\Phi = \frac{k}{k_{ref}} \frac{\int_{v_1}^{v_2} I(v) \Phi_R(v) \varepsilon_R(v) dv}{\int_{v_1}^{v_2} I(v) \varepsilon(v) dv} \quad 22$$

$$\frac{d[C]}{dt} = -k[C] \quad 23$$

The concentration change during continuous irradiation was followed by the change in absorption, knowing the individual  $\varepsilon$ , yielding the rate constants ( $k$ ).

### 3.4. Electrochemistry

Electrochemical measurements were carried out in a conventional three-electrode setup; with a working, a counter and a reference electrode; a heavy, but all-inclusive book on the subject is published by Bard and Faulkner.<sup>118</sup> Ferrocene was added subsequent to measurements and the ferrocene/ferrocenium couple ( $\text{Fc}^{0/+}$ ) was recorded as an internal standard. Two different potential step procedures were used, cyclic voltammetry (CV) and differential pulse voltammetry (DPV).

CV voltammograms were recorded by sweeping the potential linearly over complete cycles several times. For the reversible redox events, the potentials were reported as the mean value of the anodic and cathodic peak. Irreversible redox behavior were examined by DPV.

<sup>h</sup> The same equation in Paper II has a typo, where the subscript for refractive index is in the numerator.

## 3.5. Data analysis

### 3.5.1. Excited state decay fitting

Time resolved emission and transient absorption decays were fitted to exponential functions in Igor or Matlab. Most often, fitting the decays to a mono-exponential model resulted in satisfying fits:

$$I(t) = I_0 e^{-t/\tau} \quad 24$$

Where the intensity at time  $t$  ( $I(t)$ ) is related to the intensity at the time of the pulse ( $I_0$ ) and decaying with time, dependent on  $\tau$ . In the case where the pulse was only moderately shorter than the excited state decay, a deconvolution procedure was employed, using the FluoFit software package (PicoQuant).

### 3.5.2. Spectral component analysis.

The low temperature emission spectra were fitted to a series of Gaussian functions, according to the procedure of Meyer and coworkers:<sup>103, 105, 109, 119</sup>

$$I(\nu) = \sum_{n_M} \sum_{n_L} \left( \frac{E_{00} - n_M \nu_M - n_L \nu_L}{E_{00}} \right)^3 \left( \frac{S_M^{n_M}}{n_M!} \right) \left( \frac{S_L^{n_L}}{n_L!} \right) \times \left\{ \exp \left( -4 \ln 2 \left( \frac{\nu - E_{00} - n_M \nu_M - n_L \nu_L}{\nu_{1/2}} \right)^2 \right) \right\} \quad 25$$

Where  $I(\nu)$  is the intensity,  $E_{00}$  is the energy of the 0-0-transition and  $\nu_{1/2}$  is the full width at half maximum (fwhm) of the Gaussians. Subscripts M and L denotes medium and low frequency vibrational modes, and  $n_i$  is the vibrational state quantum number,  $\nu_i$  is the energy,  $S_i$  is the Huang-Rhys factor.  $S_i$  is related to the nuclear distortion between the ground and excited states, where  $S_i = \lambda_i/\nu_i$ ,  $\lambda_i$  being the reorganization energy.



## 4. Results and discussions

In the following sections, I present selected results from my studies of Ru<sup>II</sup> complexes and their structure-function relationships. I have focused on the photophysical, photochemical and electrochemical properties of the complexes, and data I have collected myself. Data relating to TD-DFT calculations and non-optical spectroscopy (NMR, MS, X-ray structures) have been collected by co-authors and are included to a lesser extent. The reader is referred to the appended papers for the structural characterization.

The research has been largely oriented toward, and motivated by, solar energy conversion; for sensitized processes (mainly DSSCs), or for photochemical energy storage. Fundamental understanding of how structure and function is coupled would allow design of complexes to increase the efficiency of the DSSC or of photocatalytic processes. For this purposes, the relevant functions of the complex are: light harvesting capabilities, the spectral shape and molar absorptivity; excited state reactivity, both in respect to specific reactions and photo-stability; emissive properties, like spectral shape, quantum yield and lifetime; and electrochemical properties, such as redox potentials for use as electron donor or acceptor.

The chapters are divided into this set of functions: 1) structures, 2) absorption and electrochemistry (ground state electronic structure), 3) excited state properties, and 4) a short summary of the study. The collected results are mainly contrasted to the prototypical [Ru(bpy)<sub>3</sub>]<sup>2+</sup> and [Ru(tpy)<sub>3</sub>]<sup>2+</sup>, as well as those mentioned in the Ru<sup>II</sup> background chapter.

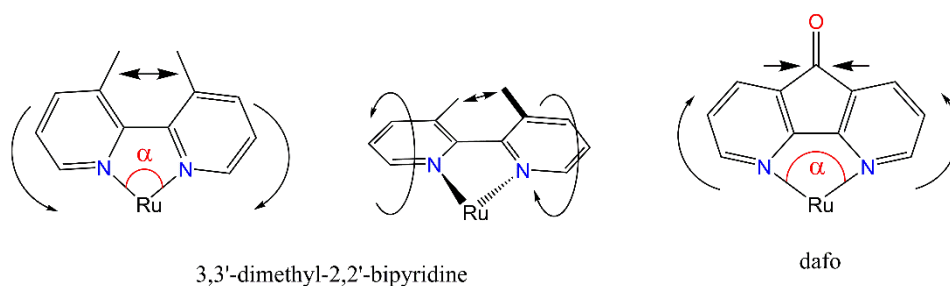
### 4.1. Coordinating 3,3'-connected ligands

This section is based on the study in Paper I, and the complexes reported therein. Additionally, femtosecond transient absorption data, not included in the publication, is presented.

#### 4.1.1. Structures

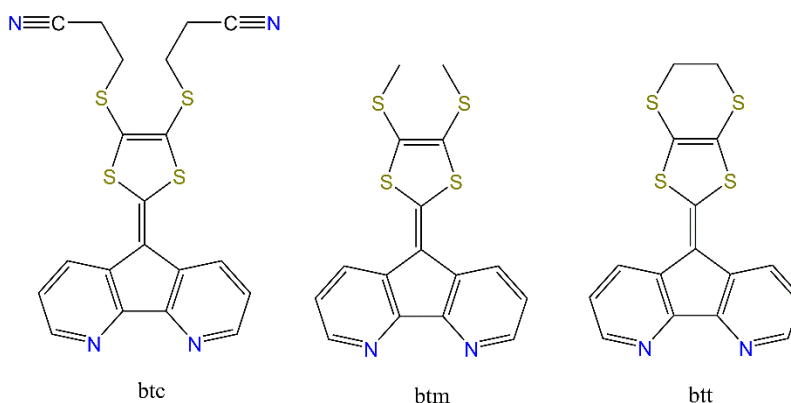
As discussed in the previous sections, substitutions to the 4,4'-positions of bpy-type ligands have been performed extensively, while similar 3,3'-substitutions have not been explored to the same extent. Substitutions in the 3,3'-positions result in large steric interactions due to the proximity of the substituents, and forces the pyridines out of plane to one another, Scheme 17. One example was presented by Chabolla et al., which compared methyl substituted bpy in the 3,3' and 5,5' positions in Rh(3,3'-methyl-2,2'-bpy)(CO)<sub>3</sub>Cl and Rh(5,5'-methyl-2,2'-bpy)(CO)<sub>3</sub>Cl. The dihedral angles were found to be 42.7 and 1.7° respectively, also substantially affecting the C-C bond length connecting the pyridine rings (1.502 vs 1.469 Å).<sup>120</sup>

Additionally, large deviations in planarity cause distorted bond lengths and dihedral angles, in turn associated with stabilized <sup>3</sup>MC states and a short lived excited state and low photostability.<sup>19, 103</sup> One way to circumvent the lost planarity can be managed by connecting the 3,3'-positions, as with a ketone, Scheme 17.<sup>121, 122</sup> By locking the 3,3'-position in relation to one-another, the pyridines are forced into the same plane. However, by connecting the back-side of the bpy-ligand, the bite-angle (N-Ru-N) is increased, due to the ketone pulling the C3's together.



**Scheme 17.** Steric interaction between 3,3'-substituents, and ligand structures of 3,3'-methyl-2,2'-bipyridine (3-dmb) and 4,5-diazafluoren-9-one (dafo).

The ketone of the dafo ligand allow for further chemical modifications, and in the study of Paper I, three derivatives were examined. These ligands all contained a dithiole motif with varying thioether substituents, btc (thio-cyano), btm (thio-methyl) and btt (thio-thio), Scheme 18. The notion btx is used to refer to all ligands. The ligands were combined with either bpy or deeb to form the six complexes,  $[\text{Ru}(\text{bpy})_2(\text{btx})]^{2+}$  and  $[\text{Ru}(\text{deeb})_2(\text{btx})]^{2+}$ , with the intent to produce high-extinction coefficient dyes for solar harvesting purposes.



**Scheme 18.** Molecular structures of 3,3'-connected (btx) ligands: btc, btm, and btt.

One of these,  $[\text{Ru}(\text{bpy})_2(\text{btc})]^{2+}$  was characterized by X-ray crystallography. The Ru-N bonds for the btc ligand were substantially longer than those for the Ru-N distances to bpy; 2.134/2.139 Å compared to 2.059/2.051 Å and 2.052/2.060 Å for the two bpy ligands. As expected, the bite-angles increased (82.5° compared to 78.5° and 78.9° for bpy), and the 3,3'-connection forced the bonds in the 5-membered ring to be contracted compared to other C-C bonds. The bpy-ligands themselves did show some deviations in bond lengths compared to  $[\text{Ru}(\text{bpy})_3]^{2+}$  (on average 2.060 Å), with a shortening of the bonds trans to btc. The similarity between the ligands in the btx-series, and the shear distance (8-bonds) to the non-equivalent parts, suggest that similar structures would be observed for the other complexes, should they form crystals. The longer bond lengths for btc can be understood in terms of both expanded bite angle, altering the orbital overlap, but also in poorer  $\pi$ -accepting capability of the ligand due to the sulfur-rich EDG.

#### 4.1.2. Absorption and electrochemical properties

The sulfur rich ligands absorbed strongly with  $\lambda_{\text{max}}$  around 400-430, with molar absorptivities on the order of  $2 \times 10^4 \text{ M}^{-1} \text{ cm}^{-1}$ . The resulting complexes also exhibited strong visible light absorption, with molar absorptivities several times larger than  $[\text{Ru}(\text{bpy})_3]^{2+}$ , Table 2 and Figure

2. TD-DFT calculations indicated that for all  $[\text{Ru}(\text{deeb})_2(\text{btx})]^{2+}$  complexes, HOMO were localized on the btx ligand, and lower lying orbitals displayed larger electron densities on the metal. The calculations displayed LUMOs that were localized on the bpy or deeb ligands respectively. Consequently, the lowest energy transition appeared as ligand-ligand transitions, followed by, at higher energies, MLCT transitions. As the remarkably strong absorption were larger than just the sum of the parts, it was ascribed to large contribution from intra-ligand as well as inter-ligand transitions on top of the MLCT absorption.

**Table 2.** Maximum absorption wavelength ( $\lambda_{\text{Abs}}$ ) and molar absorptivities ( $\epsilon$ ) for complexes with btc, btm, and btt ligands in acetonitrile at room temperature.

Compound	$\lambda_{\text{Abs}} / \text{nm}$ ( $\epsilon / \text{M}^{-1} \text{cm}^{-1}$ )	$E_{\text{Ox}} / \text{V vs Fc}^{0/+}$ <sup>a</sup>	$E_{\text{Red}} / \text{V vs Fc}^{0/+}$ <sup>a</sup>
$[\text{Ru}(\text{bpy})_2(\text{btc})]^{2+}$	468 (32 000)	+0.85	-
$[\text{Ru}(\text{bpy})_2(\text{btm})]^{2+}$	440 (31 700)	-	-
$[\text{Ru}(\text{bpy})_2(\text{btt})]^{2+}$	457 (30 200)	-	-
$[\text{Ru}(\text{deeb})_2(\text{btc})]^{2+}$	470 (44 300)	+0.88, +1.16	-1.6
$[\text{Ru}(\text{deeb})_2(\text{btm})]^{2+}$	475 (40 300)	-	-
$[\text{Ru}(\text{deeb})_2(\text{btt})]^{2+}$	483 (46 800)	-	-

<sup>a</sup> Values from reference.<sup>121</sup>

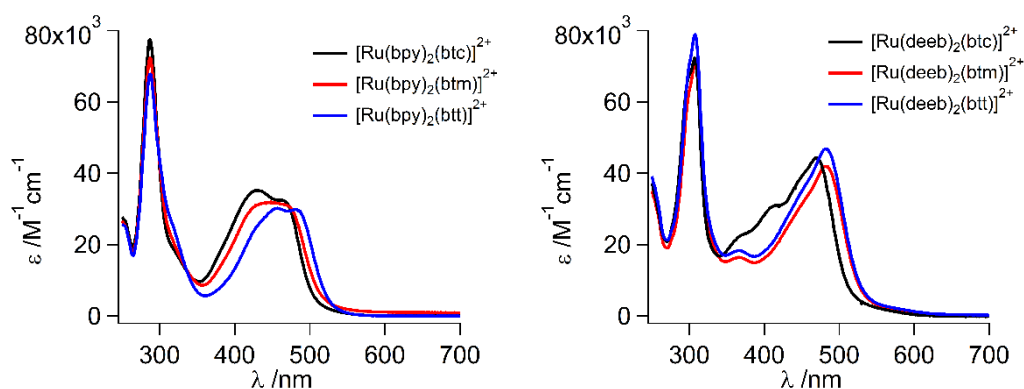


**Figure 2.** Absorption spectra of  $[\text{Ru}(\text{bpy})_2(\text{btx})]^{2+}$  (left) and  $[\text{Ru}(\text{deeb})_2(\text{btx})]^{2+}$  (right) complexes in neat acetonitrile: btx being btc, btm or btt.

While the redox properties of the complexes were not measured, a previous publication report on the electrochemistry of  $[\text{Ru}(\text{bpy})_2(\text{btc})]^{2+}$  ( $E_{\text{Ox}} +0.85$  vs  $\text{Fc}^{0/+}$ ) and  $[\text{Ru}(\text{deeb})_2(\text{btc})]^{2+}$  ( $E_{\text{Ox}} +0.88, +1.16$  and  $E_{\text{Red}} -1.6$  V vs  $\text{Fc}^{0/+}$ ) is cited.<sup>121</sup> The  $\text{Ru}^{3+/2+}$  couple for both complexes are somewhat shifted to less positive potential potentials compared to the corresponding  $[\text{Ru}(\text{N},\text{N})_3]^{2+}$ .

#### 4.1.3. Excited state properties

With expanded bite-angles, elongated Ru-N bond distances, and calculations suggesting LUMOs having little MLCT character, the excited state lifetimes were, as could be expected, short ( $< 10$  ns). Consequently, no characteristic MLCT-emission was observed at room temperature. At  $-40$  °C, the transient absorption of  $[\text{Ru}(\text{deeb})_2(\text{btm})]^{2+}$  and  $[\text{Ru}(\text{deeb})_2(\text{btt})]^{2+}$  resembled typical  $^3\text{MLCT}$  states, with ground state bleaches between 400-500 nm, a positive feature below 400 nm and a weak positive absorption above 500 nm.

This is contrasted by femtosecond transient absorption (*not included in appended papers*) on  $[\text{Ru}(\text{deeb})_2(\text{btt})]^{2+}$  in acetonitrile at ambient temperature, which displayed an intense excited state absorption centered at ca 500 nm, Figure 3. This feature decayed on similar time scale as the ground state bleach, but with different contribution to  $\Delta A$ , and became red-shifted by 10–15 nm during its bi-exponential decay.  $[\text{Ru}(\text{deeb})_2(\text{btm})]^{2+}$  displayed a similar decay but with lower intensity. This shifting of the ES absorption indicated that more than one process occurs, and the time scale is likely too long to be due to vibrational relaxation (the spectra has not been corrected for chirp,<sup>i</sup> which progressed over the full spectra in  $\sim 1$  ps).

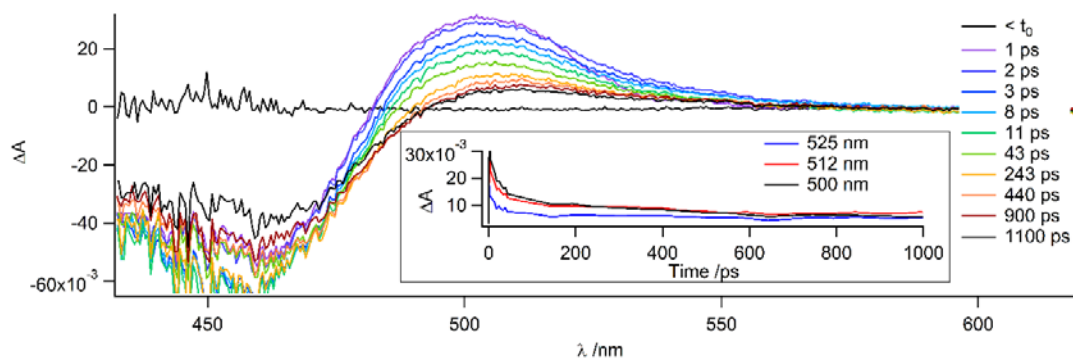


**Figure 3.** fs-TA of  $[\text{Ru}(\text{deeb})_2(\text{btt})]^{2+}$  in acetonitrile, excited at 475 nm. Inset of single wavelength kinetics. (A data point at 800 ps were removed due to pulse fall-out).

Upon further cooling to liquid nitrogen temperatures typical MLCT emission was observed for all of the complexes. For  $[\text{Ru}(\text{deeb})_2(\text{btc})]^{2+}$  the emission was characteristic of a deeb-localized MLCT emissive state, with no significant deviations in the spectral shape between the three complexes, Figure 4 and Table 3. Additionally, only minor variations in the excited state lifetimes were seen (6.1–7.3  $\mu\text{s}$ ), which is shorter than that of  $[\text{Ru}(\text{deeb})_3]^{2+}$ .<sup>18</sup> While the ester groups in deeb lowers the  $\pi^*$  levels sufficiently for the excited state to be exclusively deeb-localized, the excited state of  $[\text{Ru}(\text{bpy})_2(\text{btc})]^{2+}$  was not found to be bpy-localized. As a result, the btc and bpy ligand energies are closer spaced, in turn affecting the emission spectra. Within this series of bpy-complexes, significant dissimilarities in emission spectral shape was observed, where these complexes display more structured spectra than corresponding deeb-complexes.

**Table 3.** Emission properties of complexes with btc, btm, and btt ligands at liquid nitrogen temperatures.

Compound	<sup>a</sup> $\lambda_{\text{Em}}$ /nm	<sup>b</sup> $\tau$ / $\mu\text{s}$
$[\text{Ru}(\text{bpy})_2(\text{btc})]^{2+}$	602	6.2
$[\text{Ru}(\text{bpy})_2(\text{btm})]^{2+}$	612	5.0
$[\text{Ru}(\text{bpy})_2(\text{btt})]^{2+}$	608	3.6
$[\text{Ru}(\text{deeb})_2(\text{btc})]^{2+}$	613	6.1
$[\text{Ru}(\text{deeb})_2(\text{btm})]^{2+}$	614	7.2
$[\text{Ru}(\text{deeb})_2(\text{btt})]^{2+}$	615	7.3

<sup>a</sup> Spectra at 80 K in 2-MeTHF and <sup>b</sup> lifetime at 77 K in 1:4 MeOH:EtOH.

<sup>i</sup> Chirp is the phenomena where different wavelengths arrives at different times due to the speed of light in media being wavelength dependent.

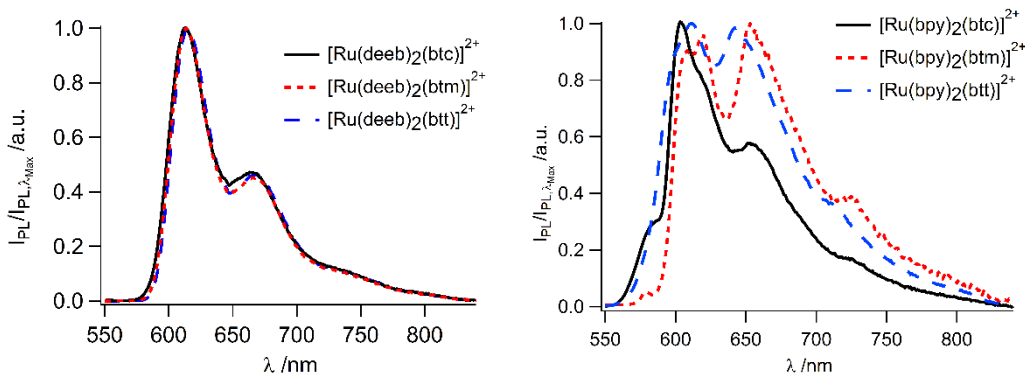


**Figure 4.** Normalized, corrected photoluminescence spectra of (left)  $[\text{Ru}(\text{deeb})_2(\text{btc})]^{2+}$  and (right)  $[\text{Ru}(\text{bpy})_2(\text{btc})]^{2+}$  complexes at 80 K in solid matrix of 2-methyl-tetrahydrofuran.

By spectral component analysis of the emission spectra for the deeb-complexes, the emission could be fitted to a series of Gaussians according to Equation 18; with  $E_{00} \sim 16\,600\text{ cm}^{-1}$ ,  $S_m \sim 0.7$ , and  $\nu_M \sim 1350\text{ cm}^{-1}$ . The vibrational progression was in line with what is typically reported for complexes similar to  $[\text{Ru}(\text{bpy})_3]^{2+}$ ;<sup>123</sup> as was also evident from inspection of the emission spectra. The red-shifted  $E_{00}$ , compared to  $[\text{Ru}(\text{bpy})_3]^{2+}$ , is also expected due to the electron withdrawing ester groups. The variation in the parameters between the complexes was within the error-margin of the procedure. However, the same could not be done for  $[\text{Ru}(\text{bpy})_2(\text{btc})]^{2+}$ ; the additional structure, compared to  $[\text{Ru}(\text{bpy})_3]^{2+}$ , would require additional vibrational modes for the model to fit, as to account for additional accepting frequencies of the less localized ES, indicated by Figure 4.

#### 4.1.3.1. Surface sensitization – Hole-transfer on $\text{TiO}_2$ films

The ester groups of the deeb ligand enabled anchoring of  $[\text{Ru}(\text{deeb})_2(\text{btc})]^{2+}$  to nanocrystalline  $\text{TiO}_2$ . Upon excitation in the visible region, electron injection into  $\text{TiO}_2$  was observed, with moderate injection yield ( $< 20\%$ ). The transient absorption spectra revealed, in addition to the expected ground state bleach, a strong transient absorption at ca 520 nm. This absorption was ascribed to the oxidized btx ligands, as assigned from a quenching study with  $[\text{Ru}(2,2'\text{-bipyrazine})_3]^{2+}$ ; where the free ligands were oxidized in solution by the excited Ru-complex and measured with transient absorption (see Paper I for details). By MLCT-excitation of  $[\text{Ru}(\text{deeb})_2(\text{btc})]^{2+}$  anchored to  $\text{TiO}_2$ , an electron is removed from the  $\text{Ru}^{2+}$ , yielding  $\text{Ru}^{3+}$ ; the hole on  $\text{Ru}^{3+}$  can subsequently be transferred to the btx ligand, explaining the strong transient absorption at 520 nm. This intra-molecular hole-transfer resulted in very long lived, non-exponential, charge separated states (present for 100's of  $\mu\text{s}$ ), which is beneficial for efficient charge collection in dye-sensitized setups.

The hole-transfer was not observed in acetonitrile at  $-40\text{ }^\circ\text{C}$ , which displayed no significant transient absorption signal around 520 nm (the transient spectra are in the SI for Paper I). However, the room temperature fs-TA did display a prominent transient absorption around 500-515 nm, on par with the ground state bleach. This suggests that rapid hole-transfer occurred at room temperature, but not in more viscous solution close to freezing, where the reorganization energy is larger.

#### 4.1.4. Short summary

Combining the btx ligands with either bpy or deeb to produce  $[\text{Ru}(\text{N,N})_2(\text{btx})]^{2+}$  substantially increases the ground state absorption compared to  $[\text{Ru}(\text{bpy})_3]^{2+}$  and  $[\text{Ru}(\text{deeb})_3]^{2+}$ , according to “*The whole is greater than the sum of its parts*”. The extended bite-angles for btx ligands and elongated Ru-N bonds, compared to the chelated bpy and deeb, suggest fast deactivation of  $^3\text{MLCT}$  states at room temperature, which was also observed. Furthermore, femtosecond transient absorption in conjunction with the results from  $\text{TiO}_2$  sensitization imply a possible deactivation of the emissive  $^3\text{MLCT}$  state by intra-molecular hole-transfer. The lack of emission at room temperature is likely due to a combination of these two factors.

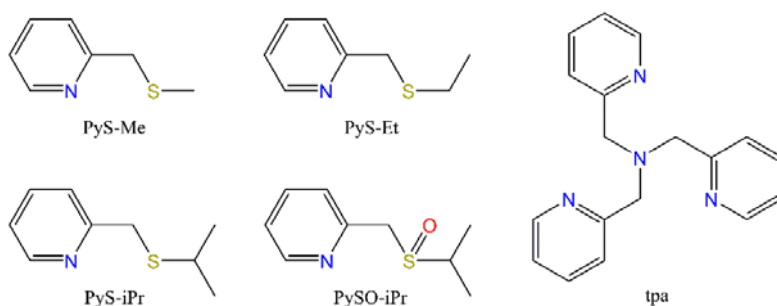
For  $[\text{Ru}(\text{bpy})_2(\text{btx})]^{2+}$ , a more delocalized excited state also preclude bpy-like  $^3\text{MLCT}$  emission, resulting in substantially more structured emission at 77 K compared to  $[\text{Ru}(\text{bpy})_3]^{2+}$ . The excited state was deeb-localized for all deeb-complexes and the emission spectra recorded at liquid nitrogen temperatures were superimposable. The similarity between the emission spectra was implying only minor perturbation from the btx ligand on the emissive state geometry at low temperatures. This suggests that btx induces larger non-radiative decay, not connected to hole-transfer, but rather resulting from the larger bite-angles and associated increase of  $^3\text{MLCT}$ - $^3\text{MC}$  surface crossing, which was further supported by the vibrational structure and predictable shift in  $E_{00}$  when compared to  $[\text{Ru}(\text{bpy})_3]^{2+}$ .

## 4.2. Coordinating sulfur-donating ligands

This section is based on the studies in Paper II and III, and the complexes reported therein.

### 4.2.1. Structures

Ligands that coordinate via nitrogen constitute the most common polydentate ligands for Ru-complexes, are the most studied and hence the most well-known. Other ligands, such as thioether coordinating motifs, have been less studied, especially photochemically. In Paper II, I have studied a set of complexes that contain such ligands, namely PyS-Me (2-[(methylthio)methyl]pyridine) and PyS-Et (2-[(ethylthio)methyl]pyridine), as well as in combinations with other ligands; either the chromophoric ligands bpy, dmb or phen, or with the non-chromophoric ligand tpa (tris(2-pyridylmethyl)amine), Scheme 19. Additional complexes,  $[\text{Ru}(\text{deeb})_2(\text{PyS-}i\text{Pr})]^{2+}$  and the corresponding sulfoxide  $[\text{Ru}(\text{deeb})_2(\text{PySO-}i\text{Pr})]^{2+}$  were also examined, and the experimental details are available in the manuscript Paper III.



**Scheme 19.** Ligand structures of sulfur donating ligands, and tetradentate tpa.

Crystal structures could be recorded for  $[\text{Ru}(\text{dmb})_2(\text{PyS-Me})](\text{PF}_6)_2$ ,  $[\text{Ru}(\text{phen})_2(\text{PyS-Me})](\text{PF}_6)_2$ ,  $[\text{Ru}(\text{tpa})(\text{PyS-Me})](\text{PF}_6)_2$ ,  $[\text{Ru}(\text{PyS-Me})_3](\text{ClO}_4)_2$  and  $[\text{Ru}(\text{PyS-Et})_3](\text{ClO}_4)_2$ ,

Figure 5. By coordinating PyS-Me in place of one of the ligands of  $[\text{Ru}(\text{dmb})_3]^{2+}$  or  $[\text{Ru}(\text{phen})_3]^{2+}$ , the coordination of the diamine ligands was not seriously perturbed, and the phen and dmb ligands displayed bite-angles between  $78.14\text{--}79.78^\circ$  and average bond lengths of ca  $2.073 \text{ \AA}$ ; somewhat longer bond-lengths but similar bite angles than for  $[\text{Ru}(\text{phen})_3]^{2+}$  ( $2.063 \text{ \AA}$  and  $79.8^\circ$ ).<sup>124</sup> The bond lengths of the pyridine in the PyS-Me ligand itself are elongated by ca  $0.03\text{--}0.04 \text{ \AA}$  compared to the Ru-N diamine bonds, and the N-Ru-S bite angles are expanded by ca  $4\text{--}5^\circ$ , ranging from  $81.5\text{--}84.0^\circ$ . The Ru-S bonds are some  $0.25 \text{ \AA}$  longer than the Ru-N bonds, approximately  $2.33 \text{ \AA}$  for the heteroleptic complexes, in line with the bond-lengths reported for the similar chelates.<sup>125</sup>

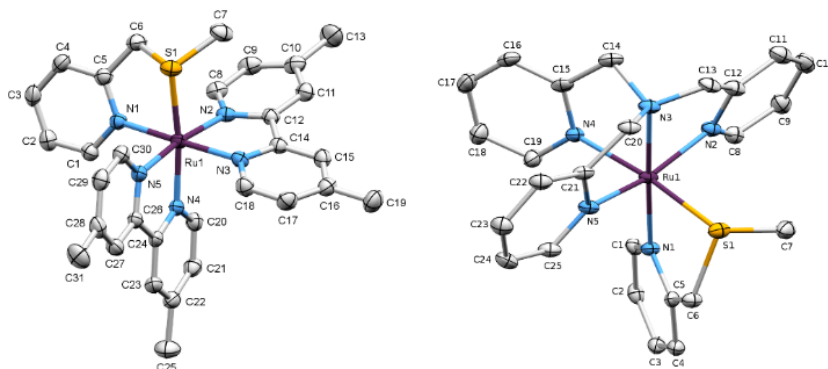


**Figure 5.** Crystal structures of  $[\text{Ru}(\text{dmb})_2(\text{PyS-Me})](\text{PF}_6)_2$  (left) and  $[\text{Ru}(\text{tpa})(\text{PyS-Me})](\text{PF}_6)_2$  (right). Hydrogen atoms omitted for clarity. Anisotropic displacement parameters drawn at the 30% probability level.

#### 4.2.2. Absorption and electrochemical properties

The  $[\text{Ru}(\text{N,N})_2(\text{PyS-Me})]^{2+}$  complexes displayed absorption spectra similar to that of the corresponding  $[\text{Ru}(\text{N,N})_3]^{2+}$ , with slightly lower molar absorptivities, Figure 6 and Table 3. While  $[\text{Ru}(\text{PyS-Me})_3]^{2+}$  and  $[\text{Ru}(\text{PyS-Et})_3]^{2+}$  had absorption bands centered at ca  $320 \text{ nm}$ , they exhibited no visible absorption and the samples were visibly transparent. The ligands themselves absorbed readily in the UV-region, centered at  $245 \text{ nm}$ , and did in this manner not contribute to the visible absorption of the complex. Reports of the complex  $[\text{Ru}(\text{bpy})_2(\text{PyS-}i\text{Pr})]^{2+}$  display similar absorption ( $\lambda_{\text{max}} 435 \text{ nm}$ ,  $\epsilon 7 580 \text{ M}^{-1}\text{cm}^{-1}$ ), slightly red-shifted compared to  $[\text{Ru}(\text{bpy})_2(\text{PyS-Me})]^{2+}$ .<sup>126</sup> Connick and coworkers have examined a series of complexes with the bis-thioether ligand dpte (1,2-bis(phenylthio)ethane) with different diimine ligands, and report  $\lambda_{\text{max}}$  values at  $404$ ,  $396$  and  $378 \text{ nm}$  for  $[\text{Ru}(\text{bpy})_2(\text{dpte})]^{2+}$ ,  $[\text{Ru}(\text{dmb})_2(\text{dpte})]^{2+}$  and  $[\text{Ru}(\text{phen})_2(\text{dpte})]^{2+}$  respectively.<sup>125</sup> Qualitatively, the blue-shifted absorption follows the number of Ru-S bonds. Similarly,  $[\text{Ru}(\text{tpa})(\text{PyS-Me})]^{2+}$  had an absorption band at  $380 \text{ nm}$ , with some tailing into the visible region, but blue-shifted compared to reports of  $[\text{Ru}(\text{bpy})(\text{tpa})]^{2+}$ .<sup>72, 127</sup> This was corroborated by the electrochemical measurements, where the HOMO-LUMO gap seen in the absorption spectra qualitatively agreed with the difference in oxidation and reduction potential of the complexes, Table 3.

#### 4. Results and discussions

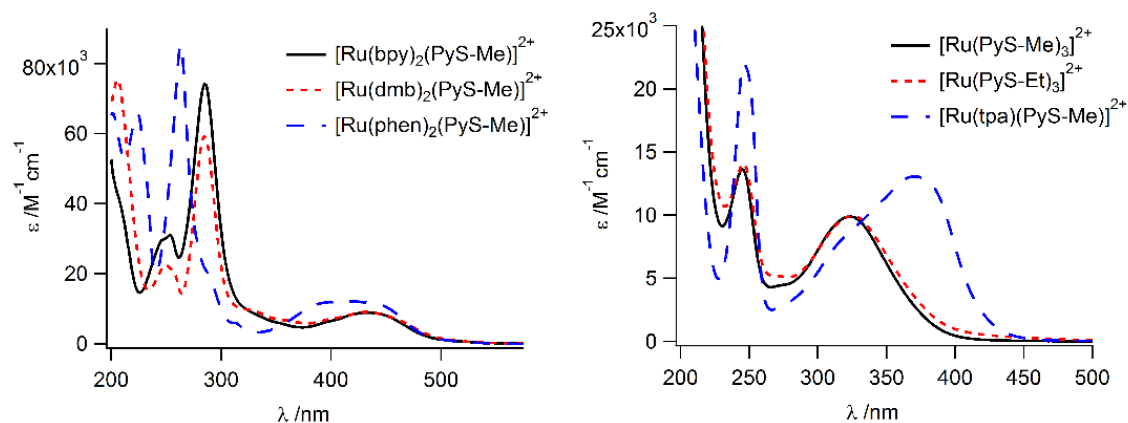


**Figure 6.** Absorption spectra of complexes with chromophoric ligands (left) and without chromophoric ligands (right).

**Table 3.** Absorption and electrochemical parameters for complexes with sulfur donating ligands at ambient temperatures.

Compound	<sup>a</sup> $\lambda_{\text{Abs}}$ /nm ( $\epsilon$ /M <sup>-1</sup> cm <sup>-1</sup> )	<sup>b</sup> $E_{\text{Ox}}$ /V vs $\text{Fc}^{0/+}$
$[\text{Ru}(\text{bpy})_2(\text{PyS-Me})]^{2+}$	432 (8 800)	1.05
$[\text{Ru}(\text{dmb})_2(\text{PyS-Me})]^{2+}$	432 (9 000)	1.01
$[\text{Ru}(\text{phen})_2(\text{PyS-Me})]^{2+}$	416 (12 100)	1.04
$[\text{Ru}(\text{tpa})_2(\text{PyS-Me})]^{2+}$	371 (13 100)	0.89
$[\text{Ru}(\text{PyS-Me})_3]^{2+}$	324 (9 900)	1.16
$[\text{Ru}(\text{PyS-Et})_3]^{2+}$	325 (9 900)	1.24

<sup>a</sup> Recorded in neat acetonitrile. <sup>b</sup> Collected in acetonitrile with 0.1 M TBAPF<sub>6</sub>,  $\text{Fc}^{0/+}$  used as internal standard.

The recorded CVs of the diimine containing complexes in connection to the recorded emission suggest that the quasi-reversible first reduction is associated with the diimine ligand, Figure 7. This is further in accordance with the absorption spectra difference between the complexes with and without chromophoric ligands.

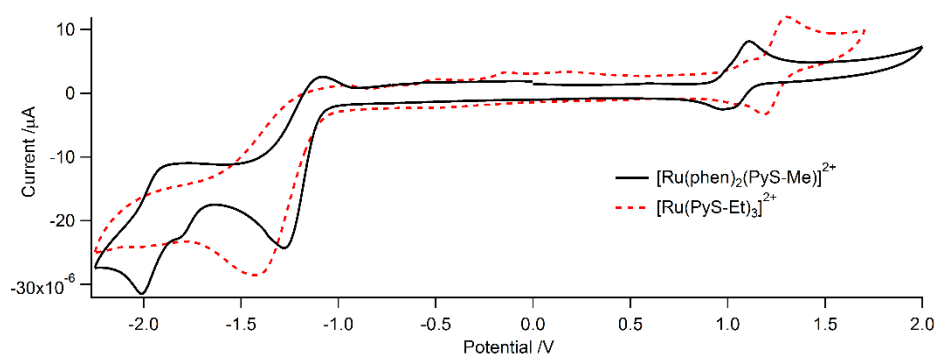


**Figure 7.** Cyclic voltammograms for  $[\text{Ru}(\text{phen})_2(\text{PyS-Me})]^{2+}$  and  $[\text{Ru}(\text{PyS-Et})_3]^{2+}$ , recorded in acetonitrile with 0.10 M TBAPF<sub>6</sub>, with  $\text{Ag}/\text{Ag}^+$  reference electrode, reported versus  $\text{Fc}^{0/+}$  internal standard.

The lower  $\pi^*$  energy of the diimine ligands result in the typical MLCT absorption, with less cluttered spectra than with btc, btm and btt, where the energy of the  $\pi^*$  system of the different ligands were more closely spaced. The oxidation potentials of the thioether complexes, especially for the homoleptic ones, were shifted to higher positive potentials, implying a decreased electron density on the Ru-centers compared to tris-diimine complexes due to sulfur coordination. The number of Ru-S bonds also tentatively follows this notion with increasing Ru<sup>3+/2+</sup> potentials.<sup>125</sup>

### 4.2.3. Excited state properties

The small perturbation to the diimine coordination, as compared to tris-homoleptic complexes, is also seen in comparing the emission spectra at room temperature between [Ru(bpy)<sub>2</sub>(PyS-Me)]<sup>2+</sup> and [Ru(bpy)<sub>2</sub>(PyS-Me)]<sup>2+</sup>, which overlaps very closely; and all [Ru(N,N)<sub>2</sub>(PyS-Me)]<sup>2+</sup> displayed typical N,N-localized <sup>3</sup>MLCT emission, Figure 8 and Table 4. However, both radiative rate constants, and especially non-radiative rate constants, are influenced by the presence of the thioether ligand, leading to a faster deactivation and a lower quantum yield. The emission was recorded in acetonitrile, methanol, dichloromethane and water, and the thioether complexes followed the solvent dependent trends of the corresponding [Ru(N,N)<sub>3</sub>]<sup>2+</sup> complexes.

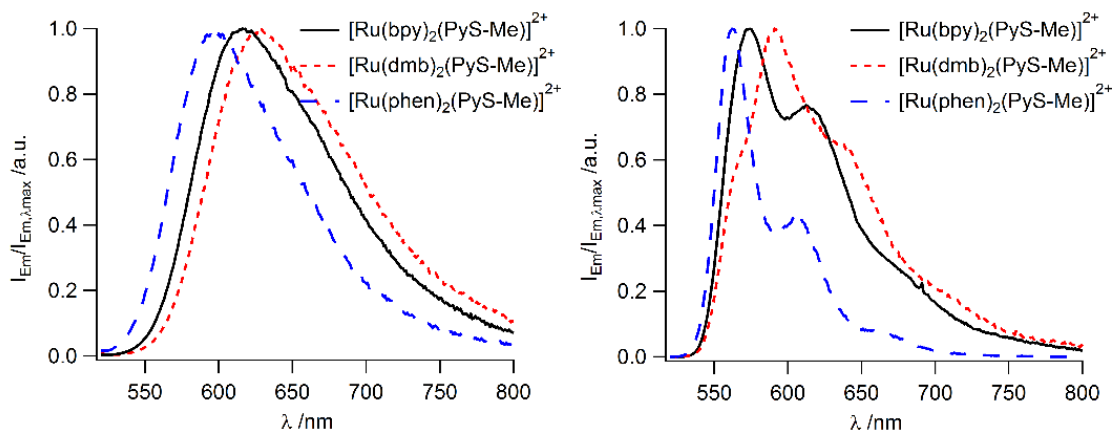


**Figure 8.** Normalized emission spectra of [Ru(N,N)<sub>2</sub>(PyS-Me)]<sup>2+</sup> complexes in acetonitrile at room temperature (left) and at 77 K in MeOH:EtOH solid matrix (right).

**Table 4.** Emission parameters for thioether complexes in neat acetonitrile at room temperature (RT) and at 77 K.

Compound	$\lambda_{Em}$ /nm RT	$\Phi$	$\tau$ / $\mu$ s RT	$\lambda_{Em}$ /nm 77 K	$\tau$ / $\mu$ s 77 K	$k_r$ /10 <sup>3</sup> s <sup>-1</sup>	$k_{nr}$ /10 <sup>6</sup> s <sup>-1</sup>
[Ru(bpy) <sub>2</sub> (PyS-Me)] <sup>2+</sup>	618	0.032	0.70	573	6.54	46	1.4
[Ru(dmb) <sub>2</sub> (PyS-Me)] <sup>2+</sup>	627	0.015	0.65	591	5.72	23	1.5
[Ru(phen) <sub>2</sub> (PyS-Me)] <sup>2+</sup>	598	0.016	0.44	562	11.1	36	2.2

Upon cooling in MeOH:EtOH (1:4), the excited state lifetimes increased rapidly in fluid solution (>110 K) and slowly in solid matrix (<110 K), Figure 9. Additionally, the unstructured <sup>3</sup>MLCT emission becomes more and more structured, and at 77 K the vibrational structure is clearly present, Figure 8.

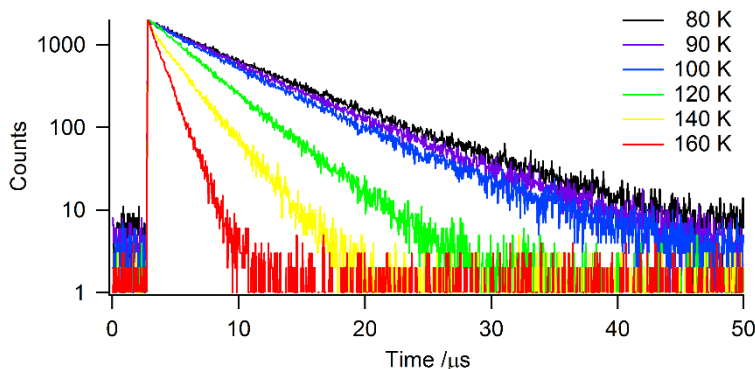


**Figure 9.** Temperature dependence of excited state lifetime of  $[\text{Ru}(\text{bpy})_2(\text{PyS-Me})]^{2+}$  in MeOH:EtOH (1:4), collected by TC-SPC.

Further credence to the (N,N)-localized excited state was provided by the results of the spectral component analysis, where both  $[\text{Ru}(\text{bpy})_2(\text{PyS-Me})]^{2+}$  (Figure 10) and  $[\text{Ru}(\text{phen})_2(\text{PyS-Me})]^{2+}$  could be nicely fitted to a series of Gaussians, Table 5. Comparing the values for the vibrational wavenumbers for the bpy-complex with that of  $[\text{Ru}(\text{bpy})_3]^{2+}$  shows minor deviations, Table 5.<sup>123</sup> The different parameters give additional information about the ground and excited states. The 0-0 transition energy ( $E_{00}$ ) is generally not directly accessible from the absorption and emission spectra for phosphorescence, or for singlet-triplet mixed emission. Additionally, the Huang-Rhys factors reflect the geometrical similarity between the vibrational structure of the excited and ground states.  $[\text{Ru}(\text{dmb})_2(\text{PyS-Me})]^{2+}$  displayed emission also from a vibrationally excited state, 1-0 transition, and could not be fitted to the same equation. However, by simulating the emission spectral components with carefully selected values, the band shape of the residual (red dashed line in Figure 10) corresponded to a slightly narrower transition than the ones originating from the relaxed excited state, in accordance with the findings of Tazuke and coworkers.<sup>128</sup>

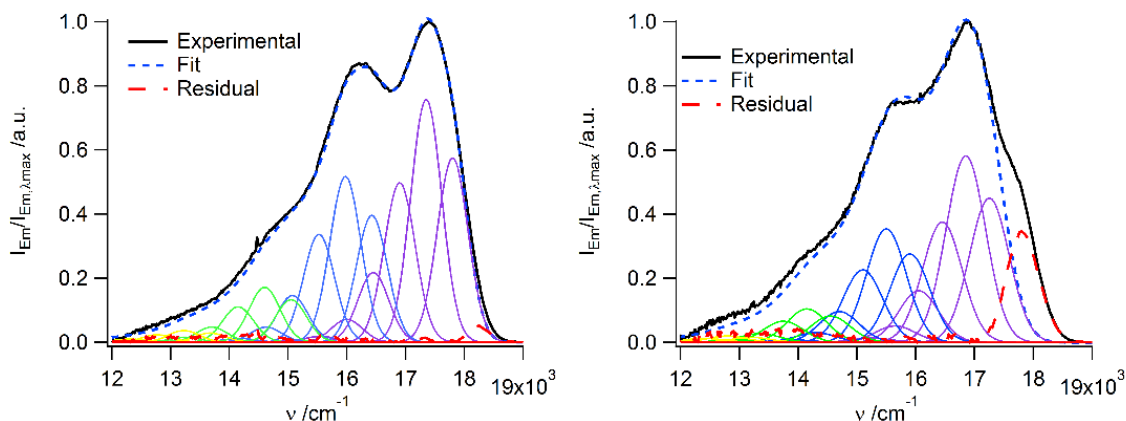


**Figure 10.** Normalized emission spectra (solid) of  $[\text{Ru}(\text{bpy})_2(\text{PyS-Me})]^{2+}$  (left) and  $[\text{Ru}(\text{dmb})_2(\text{PyS-Me})]^{2+}$  (right) at 77 K in MeOH:EtOH (1:4) solid matrix, with plotted Gaussians from spectral component analysis. Colors of Gaussians corresponds to  $n_M = 1, 2, 3, 4, 5$  (purple, blue, green, yellow, orange). Residual plotted in red/dashed.

**Table 5.** Spectral component analysis parameters of thioether complexes at 77 K in MeOH:EtOH (1:4).  $[\text{Ru}(\text{bpy})_3]^{2+}$  included from Hammarström and coworkers<sup>123</sup> for comparison.

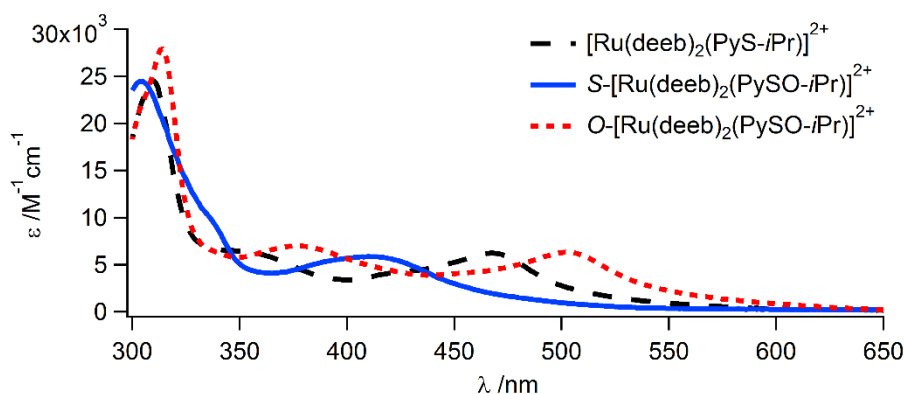
	$[\text{Ru}(\text{bpy})_2(\text{PyS-Me})]^{2+}$	$[\text{Ru}(\text{dmb})_2(\text{PyS-Me})]^{2+, \text{a}}$	$[\text{Ru}(\text{phen})_2(\text{PyS-Me})]^{2+}$	$[\text{Ru}(\text{bpy})_3]^{2+}$
$E_{00} / \text{cm}^{-1}$	17800	17250	17870	17200
$\nu_{1/2} / \text{cm}^{-1}$	620	795	723	650
$\nu_M / \text{cm}^{-1}$	1375	1350	1300	1350
$S_M$	0.95	0.85	0.63	0.87
$\nu_L / \text{cm}^{-1}$	450	400	420	N/A
$S_L$	1.46	1.42	0.57	0.97

<sup>a</sup> The data was simulated due to emission from a hot band, interfering with the fitting.

The possibility to delocalize the electron is reflected by the Huang-Rhys factors; where the numerical value of  $S_M$  was largest for phen, followed by dmb and bpy, in accordance with what would be expected. A comparison between  $[\text{Ru}(\text{bpy})_2(\text{PyS-Me})]^{2+}$  and  $[\text{Ru}(\text{bpy})_3]^{2+}$  showed smaller variations in the parameters for the energy of vibrations, Table 5.<sup>123</sup> Furthermore, the small difference in Huang-Rhys factors suggests that the GS and ES geometries are similarly distorted for both complexes, with somewhat larger value for  $S_L$  for the heteroleptic complex.

#### 4.2.3.1. Ru-sulfoxide S/O-linkage isomerization

$\text{Ru}^{\text{II}}$  complexes with sulfoxide ligands are reported to display S/O-linkage isomerization, and have been proposed for use as molecular switches, memory storage and molecular machines.<sup>129-132</sup> In applications such as molecular logic or memory storage, it is necessary to have spatial addressability, and it is thus attractive to immobilize the molecules on substrates. To this end, I examined the complex  $[\text{Ru}(\text{deeb})_2(\text{PySO-}i\text{Pr})]^{2+}$ , which can be anchored to metal-oxide substrates, such as  $\text{TiO}_2$  thin films. While no crystal structures were available, one can expect the the Ru-S bond to be shorter for the sulfoxide compared to the thioether complex; based on the report by King et al. comparing dpte with the sulfoxide analogue.<sup>133</sup>

**Figure 11.** Absorption spectra of  $[\text{Ru}(\text{deeb})_2(\text{PyS-}i\text{Pr})]^{2+}$  and  $[\text{Ru}(\text{deeb})_2(\text{PySO-}i\text{Pr})]^{2+}$  in the S- and O-bound form, recorded at ambient temperature in propylene carbonate.

Upon UV-irradiation of the S-bonded  $[\text{Ru}(\text{deeb})_2(\text{PySO-}i\text{Pr})]^{2+}$  (the thermodynamically stable isomer), the complex display light-induced linkage-isomerization, and produces the O-coordinated complex. In doing so, the absorption spectra becomes substantially red-shifted,

with maintained isosbestic points at 347, 400 and 440 nm, Figure 11. The absorption spectra of  $[\text{Ru}(\text{deeb})_2(\text{PyS-}i\text{Pr})]^{2+}$  was red-shifted compared to the sulfur bonded  $[\text{Ru}(\text{deeb})_2(\text{PySO-}i\text{Pr})]^{2+}$ ; in the same way  $[\text{Ru}(\text{bpy})_2(\text{PyS-}i\text{Pr})]^{2+}$  is red-shifted compared to  $[\text{Ru}(\text{bpy})_2(\text{PySO-}i\text{Pr})]^{2+}$ , as reported by McClure and Rack.<sup>77, 126</sup>

Following the process by UV-Vis absorption, the quantum yield of the  $\text{S} \rightarrow \text{O}$  isomerization,  $\Phi_{\text{S} \rightarrow \text{O}}$ , was estimated to 0.81. Additionally, upon 500 nm excitation of the O-bonded complex, the reversed reaction was observed, but with a much lower quantum yield of 0.013, Figure 12. For  $[\text{Ru}(\text{bpy})_2(\text{PySO-}i\text{Pr})]^{2+}$ ,  $\Phi_{\text{S} \rightarrow \text{O}}$  and  $\Phi_{\text{O} \rightarrow \text{S}}$  are reported to be 0.11 and 0.027 respectively.<sup>77</sup> An ancillary ligand that has lower lying  $\pi^*$ -levels can lower the electron density of the metal center, in effect inducing a preference for O-coordination compared to ligands with higher lying  $\pi^*$ -levels. This can explain both the higher  $\Phi_{\text{S} \rightarrow \text{O}}$  and lower  $\Phi_{\text{O} \rightarrow \text{S}}$  of  $[\text{Ru}(\text{deeb})_2(\text{PySO-}i\text{Pr})]^{2+}$  compared to  $[\text{Ru}(\text{bpy})_2(\text{PySO-}i\text{Pr})]^{2+}$ ; however, additional contributions arising from steric interactions cannot be excluded.<sup>38</sup>

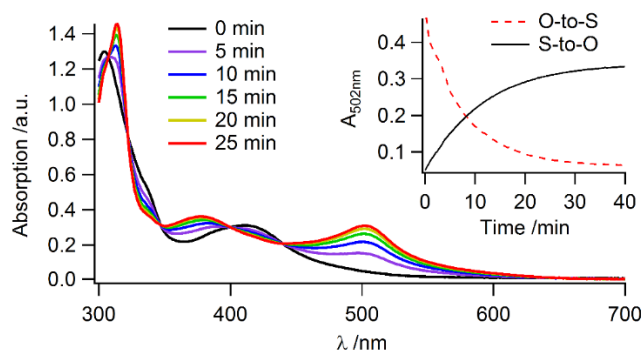


**Figure 12.** Photoisomerization of  $\text{S-}[\text{Ru}(\text{deeb})_2(i\text{Pr-PySO})]^{2+}$  in propylene carbonate irradiated with Xe-arc lamp through a 397 nm interference filter. Inset of both forward and backward process as recorded at 502 nm. Reversed process induced by Xe-arc lamp through 545 nm interference filter.

The low  $\Phi_{\text{O} \rightarrow \text{S}}$  resulted in the need for larger number of photons needed to completely reverse the process, and hence was accompanied by photo-degradation of the complex. The O-bonded complex was thermodynamically unstable, but kinetically trapped due to the large energy barrier for isomerization, and as a result the thermal reversion to the S-form in the dark proceeded to completion in ca 25 h. Similar long lifetimes have been reported several complexes, by Rack and coworkers, the most similar structurally being  $[\text{Ru}(\text{bpy})_2(\text{PySO-}i\text{Pr})]^{2+}$ .<sup>44, 77, 117</sup>

Whether or not metal-centered states are involved in S/O-isomerization is under some debate, and mechanisms both involving and excluding them are reported.<sup>78</sup> As the isomerization can be electrochemically induced, it suggests that upon MLCT absorption, the oxygen can coordinate, as sulfoxides preferentially coordinate via oxygen to  $\text{Ru}^{3+}$  and via sulfur to  $\text{Ru}^{2+}$ . However, studies observing photo-triggered S/O-isomerization in Ru complexes, but not the analogous Os complexes, where Os has less accessible  $^3\text{MC}$  states, suggest the involvement of  $^3\text{MC}$  states.<sup>77, 134</sup> In the two analogous complexes  $[\text{Os}(\text{bpy})_2(\text{PySO-}i\text{Pr})]^{2+}$  and  $[\text{Os}(\text{bpy})_2(\text{PySO-CH}_2\text{CF}_3)]^{2+}$ , only the latter one is reported to display photo-induced linkage-isomerization.<sup>134</sup> The difference was suggested to be due to the  $\text{PySO-CH}_2\text{CF}_3$  being the stronger  $\pi$ -acceptor but weaker  $\sigma$ -donor, stabilizing the  $d\pi$  orbitals and hence shifting the  $\text{Os}^{2+/+}$  couple to more positive potentials. The

difference between  $[\text{Ru}(\text{deeb})_2(\text{PySO-}i\text{Pr})]^{2+}$  and  $[\text{Ru}(\text{bpy})_2(\text{PySO-}i\text{Pr})]^{2+}$  can be explained by similar reasoning, as seen for the reduction of the corresponding  $[\text{Ru}(\text{N,N})_3]^{2+}$ , Table 1. However, the difference is induced by the ancillary ligand rather than the ambidentate ligand. Interestingly, Rack and coworkers reported on a 1-photon-2-isomerization process in  $[\text{Ru}(\text{bpy})_2(\text{L})]^{2+}$  complexes where L is dimeric in nature and have the linear formulas  $\text{Si}(\text{Me})_2(\text{CH}_2\text{SOCH}_3)_2$  (OSSO) or  $(-\text{CH}_2\text{SO}(\text{C}_6\text{H}_5\text{F}))_2$  (F-bpSO).<sup>117</sup> This kind of mechanism can be envisioned as useful in solar energy conversion or solar energy storage, as a way to circumvent the Schotcky-Queisser limit.<sup>65, 117</sup>

The anchoring of S- $[\text{Ru}(\text{deeb})_2(\text{PySO-}i\text{Pr})]^{2+}$  to nanocrystalline  $\text{TiO}_2$  thin films proceeded slowly, overnight or over several days, and displayed low final absorption. As a result, the absorption of the thin films masked most of the absorption for the sulfur-bonded isomer. However, photoinduced linkage-isomerization proceeded readily when UV-irradiated, and difference spectra displayed isosbestic points at 395 and 435 nm, ca 5 nm blueshifted to that in solution. While no quantum yield determination was performed, due to the comparably high absorption of the thin film, the O-to-S-isomerization seemed less efficient. Spectra showed that the photostationary distribution was shifted more to the O-form, suggestive of a mechanism stabilizing the  $\text{Ru}^{3+}$  state. While speculative, the blue-shifted isosbestic points in combination with a stabilized  $\text{Ru}^{3+}$  state is indicative of charge transfer to the substrate. Subsequent to electron injection, the complex features a  $\text{Ru}^{3+}$  center, favoring O-coordination. The shifted isosbestic points suggests a Stark-effect, which results in the spectra shifting as an electric potential arise due to the charge-separation.<sup>135</sup>

To investigate the electrochemically induced isomerization, electrochemical measurements of  $[\text{Ru}(\text{deeb})_2(\text{PySO-}i\text{PR})]^{2+}$  were carried out in propylene carbonate (0.1 M tetrabutylammonium hexafluorophosphate), but the oxidation features were partially masked by the solvent electrochemical window. As CVs displayed high background currents compared to the redox response from the complex, DPV was carried out instead. DPV showed that the forward oxidation of the S-bonded complex occurred at ca 1.43 V vs  $\text{Fc}^{0/+}$ , and this feature being the only one in the first run. Upon consecutive runs from 0 to 1.6 V a peak at 0.86 V vs  $\text{Fc}^{0/+}$  grew in, attributed to the O-bonded complex; after 2-3 scans, the increase in the peak current of the new feature leveled off. Upon reduction of the complex, two forward peaks appeared at ca -1.2 and -1.4 V respectively. Additionally, the feature at 0.86 V was to a large extent diminished by the reduction. The corresponding thioether complex displayed a clear forward oxidation peak at 0.90 V vs  $\text{Fc}^{0/+}$  and reductions at -1.4 and -1.6 V, and no additional features upon subsequent measurements.  $[\text{Ru}(\text{bpy})_2(\text{PySO-}i\text{Pr})]^{2+}$  is in comparison reported to have a 0.6 V separation between the O- $\text{Ru}^{3+/2+}$  and S- $\text{Ru}^{3+/2+}$  potentials, similar to that of  $[\text{Ru}(\text{deeb})_2(\text{PySO-}i\text{Pr})]^{2+}$ .<sup>77</sup> Several dmsO-complexes have displayed similarly large shifts of several hundred mV.<sup>75, 94</sup>

#### 4.2.4. Short summary

Coordination of the non-chromophoric PyS-Me to heteroleptic complexes with the classical diimine ligands dmb and phen did not perturb the geometric structure to a great extent compared to  $[\text{Ru}(\text{N,N})_3]^{2+}$ . A ca 0.01 Å elongation of the Ru- $\text{N}_{\text{N,N}}$  bond lengths was observed, but with maintained bite-angles. The Ru-S bonds were as expected substantially longer compared to the Ru-N bonds, both in comparison to the Ru- $\text{N}_{\text{N,N}}$  and Ru- $\text{N}_{\text{PyS-Me}}$ . While no crystals suitable for

diffraction could be grown for  $[\text{Ru}(\text{bpy})_2(\text{PyS-Me})]^{2+}$ , there was no reason to assume it would differ greatly from the ones that were measured.

The absorption spectra were similar to those of the corresponding  $[\text{Ru}(\text{N,N})_3]^{2+}$  in shape, but blue-shifted, an effect of increasing the HOMO-LUMO gap upon sulfur-coordination. Electrochemically, the  $\text{Ru}^{3+/2+}$  couples were shifted to more positive potentials compared to the parental diimine-complexes, in agreement with the absorption spectra. All  $[\text{Ru}(\text{N,N})_2(\text{PyS-Me})]^{2+}$  complexes were emissive at room temperature, with typical diimine localized  $^3\text{MLCT}$  emission spectra, very much resembling the shape of the corresponding  $[\text{Ru}(\text{N,N})_3]^{2+}$  emission spectra, but with slightly red-shifted emission.

For the bpy-complexes,  $E_{00}$  was  $\sim 600\text{ cm}^{-1}$  lower for the thioether complex than for  $[\text{Ru}(\text{bpy})_3]^{2+}$ , while other parameters from the spectral component analysis were relatively similar. The largest deviations are observed for  $S_L$ , suggesting perturbed low frequency Ru-N modes upon S-coordination. While the shape of emission spectra were very similar to the related  $[\text{Ru}(\text{N,N})_3]^{2+}$  complexes, the quantum yields and lifetimes were typically lower and shorter respectively. Comparing the radiative and non-radiative rate constants of  $[\text{Ru}(\text{bpy})_2(\text{PyS-Me})]^{2+}$  ( $k_r$   $46 \times 10^3\text{ s}^{-1}$ ,  $k_{nr}$   $1.4 \times 10^6\text{ s}^{-1}$ ) and  $[\text{Ru}(\text{bpy})_3]^{2+}$  ( $k_r$   $66 \times 10^3\text{ s}^{-1}$ ,  $k_{nr}$   $1.1 \times 10^6\text{ s}^{-1}$ ) shows that the chelation of the PyS-Me ligand both decreases the radiative and increases the non-radiative decay. The expected increase in structure and blue-shift of emission spectra was observed upon cooling to liquid nitrogen temperature, as well as substantially increased lifetimes.

The sulfoxide complex  $[\text{Ru}(\text{deeb})_2(\text{PySO-}i\text{Pr})]^{2+}$  displayed efficient S-to-O isomerization, while the reverse process were substantially less efficient. A higher  $\text{Ru}^{3+/2+}$  potential for this complex compared to the analogous bpy-complex explained the large difference in the quantum yield of isomerization, both for the S-to-O and the O-to-S process. The O-to-S photoinduced isomerization was less efficient when the complex was immobilized on  $\text{TiO}_2$  thin films, likely as a result of stabilizing the  $\text{Ru}^{3+}$  oxidation state.

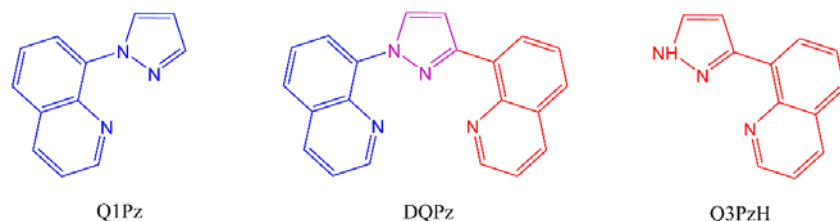
### 4.3. Coordinating quinoline-pyrazole ligands

This section is based on the studies in Paper IV, V, VI and VII, and the complexes reported therein.

#### 4.3.1. Structures

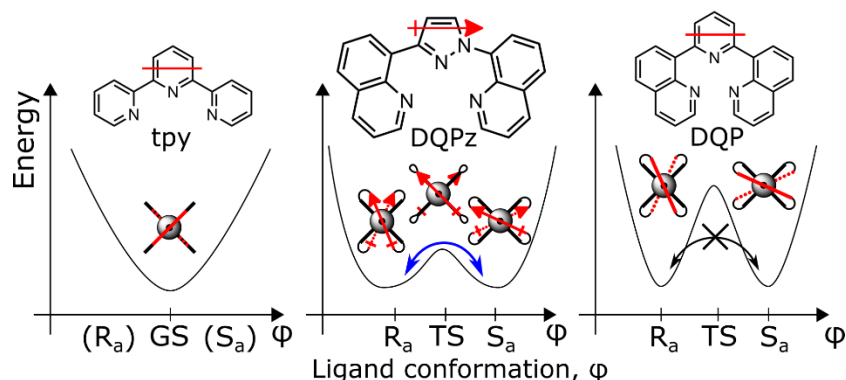
As mentioned in the background, the bulky 8-QPy ligand precludes formation of the homoleptic complex due to large steric interactions between the ligands. By replacing the pyridine in 8-QPy with the smaller pyrazole, forming Q3PzH or Q1Pz (Q3PzH is 8-(3-pyrazolyl)-quinoline and Q1Pz is 8-(1-pyrazolyl)-quinoline, Scheme 20), the inter-ligand steric interaction is decreased and the homoleptic complexes  $[\text{Ru}(\text{Q3PzH})_3]^{2+}$  and  $[\text{Ru}(\text{Q1Pz})_3]^{2+}$  can be synthesized. Additionally, the synthesis of the tridentate ligand DQPz was performed to complete the series of ligand, where DQPz can be seen as the superposition of Q3PzH and Q1Pz, illustrated by the coloring in Scheme 20. Q1Pz and Q3PzH ligands differs in the orientation between the pyrazole and quinoline motifs. The DFT calculated structures of the *mer*-isomers of the bidentate complexes display substantially shorter Ru-N<sub>Pyrazole</sub> ( $R_{\text{Pz}}$ ) bond lengths compared to Ru-N<sub>Quinoline</sub> ( $R_{\text{Q}}$ ), by ca  $0.07\text{ \AA}$ , which is suggested to be due to pyrazole

being the stronger  $\sigma$ -donor, while weaker  $\pi$ -acceptor (see Paper VI for complete lists of bond-lengths and  $-\text{angles}$ ).<sup>136</sup> In  $[\text{Ru}(\text{DQPz})_2]^{2+}$ , the difference between  $R_Q$  and  $R_{Pz}$  is even larger, ca 2.10 and 2.00 Å respectively, where the middle coordination bond appears to be compressed by the chelation of the tridentate ligand. The optimized ground state geometry of  $[\text{Ru}(\text{Q3PzH})_3]^{2+}$  reproduced the crystal structure well, suggesting that the calculated geometries of the Q1Pz and DQPz complexes are also being well represented by the calculations. The notation QPz will be used to refer to Q1Pz, DQPz and Q3PzH as a group. All complexes display more perfect octahedral geometries than complexes such as  $[\text{Ru}(\text{bpy})_3]^{2+}$  and  $[\text{Ru}(\text{tpy})_3]^{2+}$ .



**Scheme 20.** Chemical structures of quinoline-pyrazole ligands. Colors are used to illustrate similarities between Q1Pz (blue), Q3PzH (red) with DQPz (blue, red and similarity with both, purple).

Coordination of these bidentate unsymmetric ligands to Ru give rise to two isomers, *mer* and *fac*, where the *mer* isomers are the thermodynamically favored ones, as determined from calculations as well as indicated by the synthesis outcome. However, the interconversion between the two forms is not observed at ambient temperature, and the *fac* isomer is kinetically stable, and both isomers are products in the synthesis. The ligands in  $[\text{Ru}(\text{DQPz})_2]^{2+}$  are twisted, and are hence diastereotopic,<sup>j,17</sup> resulting in an additional isomer pair. These two diastereomers of the *mer* isomer, denoted C- $R_a$  and C- $S_a$  (and their respective enantiomers A- $S_a$  and A- $R_a$ ), Scheme 21, display a dynamic equilibrium at room temperature, with an exchange rate constant ( $k_{ex}$ ) of  $3.9 \text{ s}^{-1}$ ; which is not observed for  $[\text{Ru}(\text{tpy})_2]^{2+}$  or  $[\text{Ru}(\text{DQP})_2]^{2+}$ . The diastereomerization proceeded without any bond breaking. The experimental work was performed on the mixture of these two isomers, in roughly equal proportions.



**Scheme 21.** Relative transition state energy barrier for diastereomerization of homoleptic Ru complexes with tpa, DQPz and DQP ligands. Arrows indicate the observed pathways at room temperature.

<sup>j</sup> “Constitutionally equivalent atoms or groups of a molecule which are not symmetry related.” – the Gold Book, IUPAC

### 4.3.2. Absorption and electrochemical properties

As the two isomers of the bidentate complexes exhibit different geometric and electronic configurations, the photophysical and photochemical properties varies between them. This is observed in the UV-Vis spectra of the complexes, where a mixture of *mer:fac*-[Ru(Q3PzH)<sub>3</sub>]<sup>2+</sup> (3:1) display a red-shifted spectra compared to the pure *mer* sample. This redshift of the *fac*-isomer is also seen in the TD-DFT calculations, see Paper III. Furthermore, the difference in photostability between the isomers is utilized in the syntheses of the pure *mer*-isomers, where the *fac* isomers are rapidly decomposed by visible light irradiation, and consequently removed during workup, circumventing tedious isomer separations. Unless specifically stated, the complexes from here on refers to the *mer* isomers. The spectra of the two complexes were similar in acetonitrile, but with [Ru(Q3PzH)<sub>3</sub>]<sup>2+</sup> shifted to longer wavelengths for the MLCT band and shorter wavelengths for the LC-transitions, Figure 13 and Table 7.

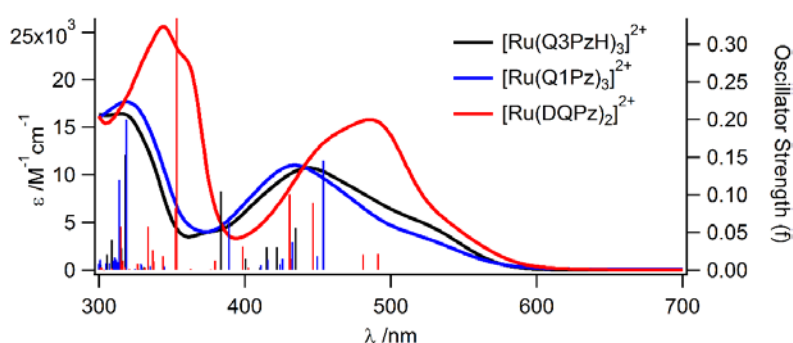


**Figure 13.** Experimental UV-Vis absorption spectra of quinoline-pyrazole complexes in neat acetonitrile and calculated oscillator strengths.

**Table 7.** Electrochemically and spectroscopically measured parameters.

Compound	<sup>a</sup> λ <sub>Abs</sub> /nm (ε /M <sup>-1</sup> cm <sup>-1</sup> )	<sup>b</sup> E <sub>Ox</sub> /V vs Fc <sup>0/+</sup> (ΔE /mV)	<sup>b</sup> E <sub>Red</sub> /V vs Fc <sup>0/+</sup>
[Ru(Q3PzH) <sub>3</sub> ] <sup>2+</sup>	444 (10 700)	0.57 (60)	-1.46, -1.89
[Ru(Q1Pz) <sub>3</sub> ] <sup>2+</sup>	434 (11 000)	0.69 (64)	-1.66, -1.84
[Ru(DQPz) <sub>2</sub> ] <sup>2+</sup>	486 (15 800)	0.65 (63)	-1.56, -1.74

However, in MeOH:EtOH at room temperature, [Ru(Q3PzH)<sub>3</sub>]<sup>2+</sup> was substantially red-shifted, with a broad, unstructured absorption band displaying a shoulder at ca 600 nm, ascribed to the protolyzable proton in Q3PzH. The red-shifted absorption in acetonitrile was qualitatively corroborated by the electrochemical measurements, where the difference in Ru<sup>3+/2+</sup> and Ru<sup>2+/+</sup> potentials for [Ru(Q3PzH)<sub>3</sub>]<sup>2+</sup> was ca 2.03 V, which is smaller than the 2.35 V for [Ru(Q1Pz)<sub>3</sub>]<sup>2+</sup>, Table 7. Calculated Ru<sup>3+/2+</sup> potentials were ca 40 mV more positive than the experimental for the bidentate complexes. [Ru(DQPz)<sub>2</sub>]<sup>2+</sup> displayed a substantially red-shifted and more prominent absorption spectra, despite the larger potential gap between Ru<sup>3+/2+</sup> and Ru<sup>2+/+</sup> compared to [Ru(Q3PzH)<sub>3</sub>]<sup>2+</sup>.

### 4.3.2.1. $[\text{Ru}(\text{Q3PzH})_3]^{2+}$ proton sensitivity

The protolyzable hydrogen in  $[\text{Ru}(\text{Q3PzH})_3]^{2+}$  results in sensitivity toward the presence or absence of protons. Upon deprotonation, the spectra becomes red-shifted with each consecutive removed proton, Figure 14. By accumulating charge on the deprotonated ligands, metal center HOMO becomes destabilized, resulting in the observed red-shift, as predicted by TD-DFT calculations. Each specific deprotonation results in a slightly different spectra due to the non-degenerate ligands. This effect cannot be observed by experiments in solution, and the unique deprotonations were evaluated by TD-DFT, Figure 14. The  $\text{pK}_{\text{a}1}$  and  $\text{pK}_{\text{a}2}$  were determined to be 8.7 and 10.7 respectively, by monitoring the pH and absorption spectra simultaneously.

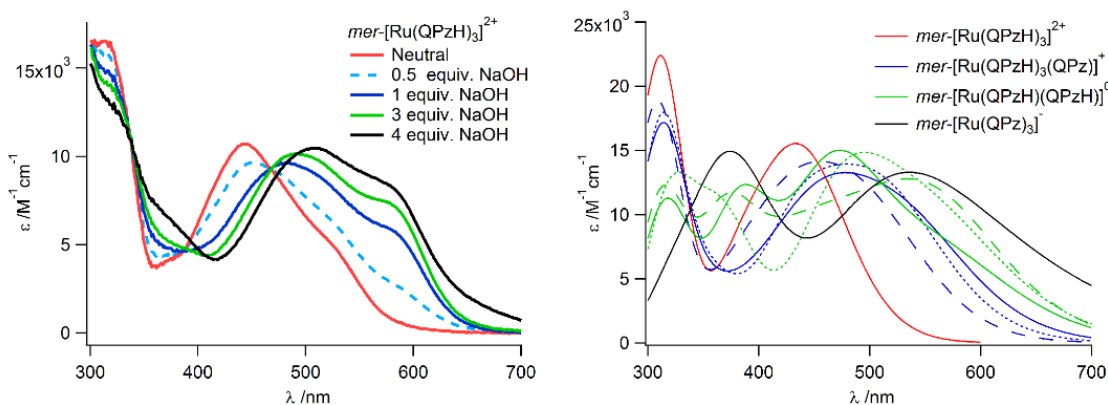


**Figure 14.** UV-Vis spectra following the deprotonation of  $\text{mer-}[\text{Ru}(\text{Q3PzH})_3]^{2+}$  upon base titration in acetonitrile (left), and TD-DFT calculated UV-Vis spectra for  $\text{mer-}[\text{Ru}(\text{Q3PzH})_3]^{2+}$  and all unique deprotonations.

### 4.3.3. Excited state properties

None of the three QPZ complexes display any room temperature photoluminescence in steady-state experiments ( $\Phi_{\text{PL}} < 0.01\%$ ), and displayed pulse-limited responses in TC-SPC measurement (pulse fwhm  $\sim 70$  ps). The fast deactivation of the excited states is not surprising in light of the calculated relative energies between the  $^3\text{MLCT}$  and  $^3\text{MC}$  states, where the non-emissive metal-centered states are all lower in energy than their MLCT counterpart (see Paper VII).

Populating the  $^3\text{MC}$  states was predicted by the TD-DFT to be accompanied by large nuclear coordinate distortion, Figure 15, with average Ru-N bond length elongation by  $\sim 0.14$  Å compared to the GS for the bidentate complexes, and  $\sim 0.09$  Å for the tridentate complex. For the bidentate complexes, the bond elongation for *mer* was predominantly seen in the quinoline coordinate, while for *fac* all Ru-N bond lengths were increased substantially, explaining the lower photostability of the latter (*fac*-isomers was removed in the synthesis by white-light irradiation). The much longer bonds in  $^3\text{MC}$  result in photoinduced ligand dissociation, which is discussed below.

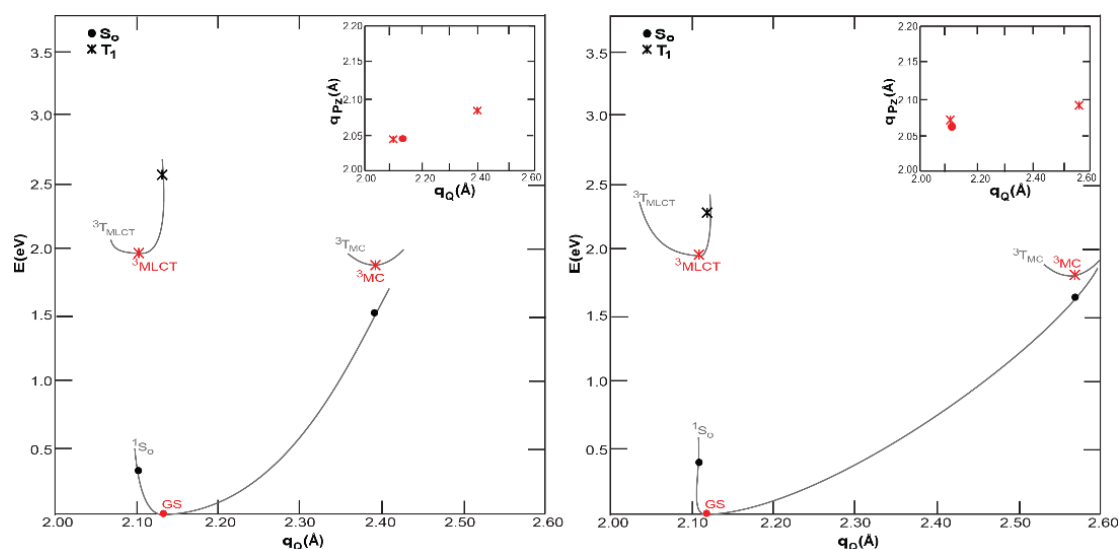


**Figure 15.** Calculated projected potential energy surfaces on the Ru-Q coordinate for  $[\text{Ru}(\text{Q3PzH})_3]^{2+}$  (left) and  $[\text{Ru}(\text{Q1Pz})_3]^{2+}$  (right). Inset of both Ru-Pz and Ru-Q distances for the minima location.

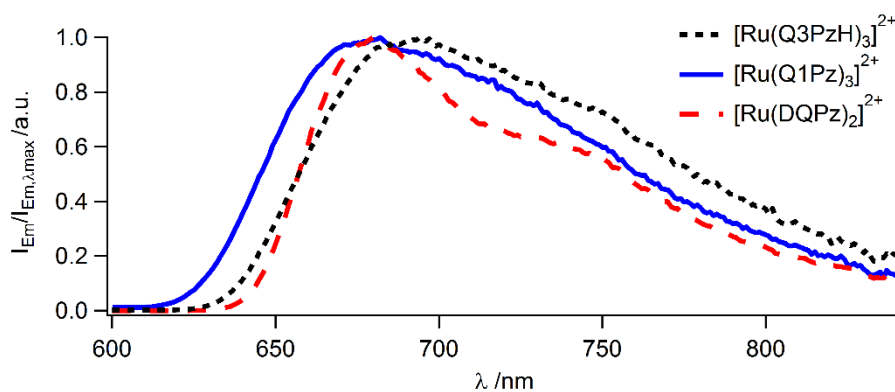


**Figure 16.** Normalized, corrected emission spectra of quinoline-pyrazole complexes in MeOH:EtOH (1:4, v:v) solid matrix at 77 K.

Upon cooling to  $\sim 160$  K, the emission from the complexes became detectable. At 77 K, typical  $^3\text{MLCT}$  emission was observed with  $\lambda_{\text{max}}$  at 696, 676, and 680 nm for  $[\text{Ru}(\text{Q3PzH})_3]^{2+}$ ,  $[\text{Ru}(\text{Q1Pz})_3]^{2+}$ , and  $[\text{Ru}(\text{DQPz})_2]^{2+}$  respectively, Figure 16 and Table 8. The notion of  $^3\text{MLCT}$  photoluminescence was corroborated by the transient absorption spectra, which displayed the expected ground state bleach, and positive transient absorption signals at ca 370-410 nm and 570-630 nm. For each complex, the single wavelength traces for the ground state bleach and the positive transient absorption at ca 400 nm could be fitted to a monoexponential function with microsecond lifetimes, with self-consistent values for the excited state lifetime, Figure 17 and Table 8.

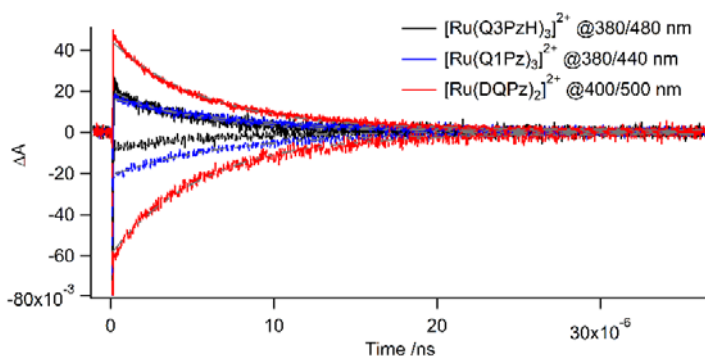


**Figure 17.** Nanosecond transient absorption traces of QPz-complexes at 77 K in MeOH:EtOH (1:4) at indicated wavelengths.

**Table 8.** Photophysical parameters for complexes with quinoline-pyrazole ligands at 77 K in MeOH:EtOH (1:4) solid matrix. Maximum intensity emission wavelength ( $\lambda_{Em}$ ), lifetime ( $\tau$ ), quantum yield ( $\Phi$ ), radiative ( $k_{rad}$ ) and non-radiative rate constants ( $k_{nr}$ ).

Compound	$\lambda_{Em}/nm$	$\tau/\mu s$	$\Phi$	$k_{rad}/\times 10^3 s^{-1}$	$k_{nr}/\times 10^6 s^{-1}$
$[Ru(Q3PzH)_3]^{2+ a}$	696	4.99	0.007	1.40	0.199
$[Ru(Q1Pz)_3]^{2+ a}$	676	7.06	0.014	1.98	0.140
$[Ru(DQPz)_2]^{2+ a}$	680	5.73	0.038	6.63	0.168

The complexes displayed very low photoluminescence quantum yields even at liquid nitrogen temperature; and with reasonably long lived excited states, this resulted in low radiative rate constants, Table 8. Both tris-bidentate complexes exhibited substantially smaller  $k_{rad}$  than the bis-tridentate complex, by a factor of 4, qualitatively in line with what could be estimated by a first approximation from the absorption spectra. The spread in  $k_{nr}$  was comparably small.

**Table 9.** Spectral component fit parameters at 77 K in MeOH:EtOH for QPz-complexes.  $[Ru(bpy)_2(8-QPy)]^{2+}$  added for comparison.<sup>112</sup>

	$[Ru(Q3PzH)_3]^{2+}$	$[Ru(Q1Pz)_3]^{2+}$	$[Ru(DQPz)_2]^{2+}$	$[Ru(bpy)_2(8-QPy)]^{2+}$
$E_{00}/cm^{-1}$	15050	15269	14827	15 540
$\nu_{1/2}/cm^{-1}$	1346	1479	1326	1230
$\nu_M/cm^{-1}$	1319	1263	1368	1350
$S_M$	0.813	0.851	0.682	0.91
$\nu_L/cm^{-1}$	457	452	604	400
$S_L$	1.924	1.677	0.882	0.83

Spectral component analysis of the emission spectra recorded at 77 K for the QPz-complexes displayed very large  $\nu_{1/2}$  for all complexes, ranging from ca 1300-1500  $cm^{-1}$ , which is indicated by the broad unstructured spectra in Figure 16. It is natural that the larger  $\pi^*$  system of the QPz-ligands, compared to the complexes with diimine ligands in the previous section, induces a broadening presumably due to a larger range of accessible nuclear configurations. This is also seen for  $[Ru(bpy)_2(8-QPy)]^{2+}$ , which was ascribed to inter-ligand steric interactions, likely applicable also to the QPz-series.<sup>112</sup> The comparably lower value of  $S_M$  for  $[Ru(DQPz)_2]^{2+}$  is qualitatively predicted by the more narrow PPES. The low frequency vibration of the tridentate

complex is higher than those of the bidentate ones, possibly arising due to the compressed Ru-N<sub>Pz</sub> bond.

#### 4.3.3.1. Photochemical reactions – Ligand exchange reactions

The bidentate QPz-complexes both exhibited ligand loss reactions upon irradiation. In acetonitrile the ligand-solvent exchange reaction proceeded within minutes with high intensity irradiation in the visible region. While the reactions were sporadic and without clear isosbestic points, the addition of triflic acid (an inert acid) made the reactions clean and irreversible. The constitution of the photo-products was monitored with high-resolution mass spectrometry as well as <sup>1</sup>H-NMR, which confirmed the coordination of acetonitrile, while triflic acid did not coordinate (Paper VI). The irreversibility was suggested to be due to protonation and consequently stabilization of a partially ejected ligand. By protonating the ejected, uncoordinated nitrogen, both re-coordination and di- or polymerization mechanisms<sup>k,115</sup> are blocked. Similarly, upon addition of HCl, the bidentate complexes rapidly displayed photoinduced red-shifts accredited to chlorination, Figure 18.<sup>18</sup>

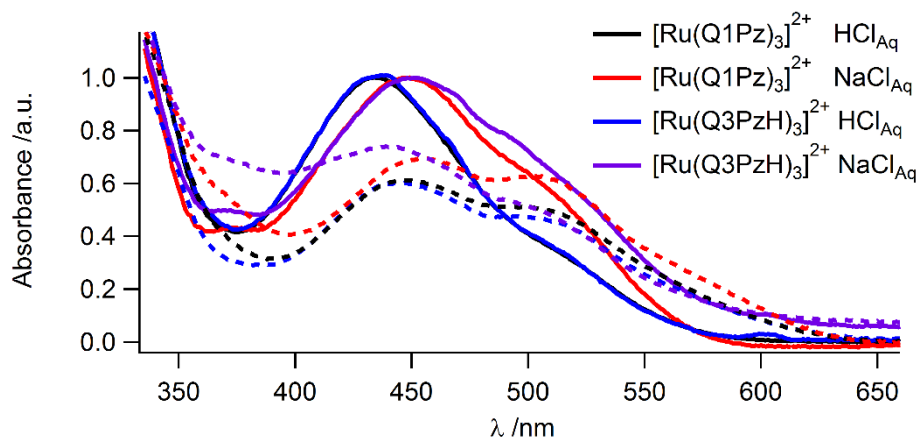


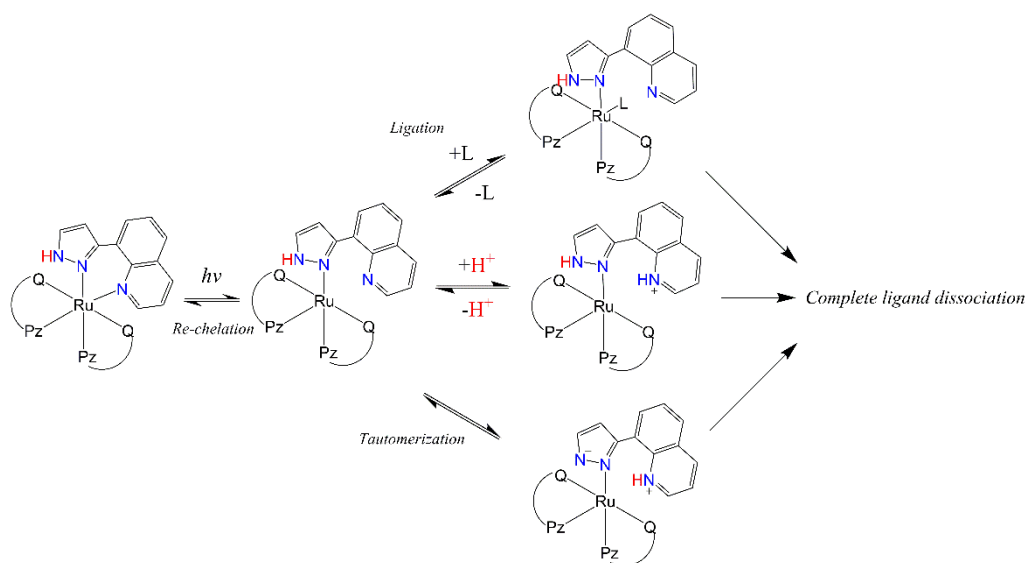
**Figure 18.** Photoreactions with NaCl<sub>Aq</sub> and HCl<sub>Aq</sub> for bidentate QPz complexes.

[Ru(Q3PzH)<sub>3</sub>]<sup>2+</sup> displayed a concentration dependent photochemical chlorination, both in spectral shape and in rates, ranging from 0.0001–0.1 M HCl, while [Ru(Q1Pz)<sub>3</sub>]<sup>2+</sup> did not. The data could not be fitted to a kinetic model of zeroth, first or second order. Instead, a combination of the reaction rates of the 5-coordinated complex must be considered, Scheme 22. The rate constants of re-chelation, protonation, solvent ligation, tautomerization, and complete ligand dissociation, and the corresponding reverse reactions, are all contributing to the overall rate and the final photoproduct composition, Scheme 22. While the short Ru-N<sub>Pz</sub> bond lengths compared to Ru-N<sub>Q</sub>, in both of the ground and <sup>3</sup>MC states, suggests that quinoline is more prone to photodissociate than pyrazole, the photodissociation of pyrazole as the initial step cannot be excluded with the data at hand. No further experiments were carried out to pin-point these rates. Studies of ligand photodissociation have displayed large variations depending on both ancillary ligand bulkiness and σ- and π-donor strengths.<sup>38</sup> One of these examples has been reported by Turro and coworkers, where [Ru(tpy)(bpy)(py)]<sup>2+</sup> displays a 3 order of magnitude lower quantum yield of photodissociation compared to [Ru(tpy)(2,2'-dimethyl-bpy)(py)]<sup>2+</sup>, ascribed by the

<sup>k</sup> Not including dimerization due to outer sphere interactions, like the hydrogen bonding dimerization reported by Metherell et al. for [Ru(PyPz)<sub>3</sub>]<sup>2+</sup>.

weakened  $\sigma$ -bonding and  $\pi$ -backbonding in the sterically hindered ancillary 2,2'-dimethylbpy.<sup>38</sup>

However, the  $\text{Cl}^-$  source mattered, where  $[\text{Ru}(\text{Q1Pz})_3]^{2+}$  displayed similar behavior in the presence of NaCl and HCl,  $[\text{Ru}(\text{Q3PzH})_3]^{2+}$  did not. The resulting spectra for the latter one with NaCl instead became blue-shifted, as in the ligand-solvent exchange in acetonitrile. The difference in photochemical selectivity between the two complexes supposedly arises due to inherent differences in reaction rates for the different reactions in Scheme 22. While further experiments are needed to extract the values of the rate constants, such selectivity is important in photochemical, and possibly in photocatalytical, applications.  $[\text{Ru}(\text{DQPz})_3]^{2+}$  did not display any significant light induced absorption changes, and was essentially unaffected in acetonitrile in presence of triflic acid even beyond one million excitation cycles.



**Scheme 22.** Possible photochemical pathways for  $[\text{Ru}(\text{Q3PzH})_3]^{2+}$ : Photoinduced partial ligand dissociation and thermal re-chelation to yield starting complex, ligation of molecule/ion (L), protonation/deprotonation of un-coordinated nitrogen, tautomerization, and complete ligand dissociation. Pathways between protonated, tautomer and ligated complexes omitted for clarity.

#### 4.3.4. Short summary

The different pyrazole-quinoline orientation in homoleptic complexes of Q3PzH and Q1Pz results in substantially different properties, most so for the oxidation and reduction potentials, and in photochemical response. The smaller group, pyrazole compared to pyridine, allowed for homoleptic complexes to be synthesized, as the steric interaction between ligands would be smaller compared to the hypothetical  $[\text{Ru}(\text{8-QPy})_3]^{2+}$ . All three QPz-complexes lacked room temperature emission, and even at low temperature quantum yields were one order of magnitude lower compared to related complexes, such as  $[\text{Ru}(\text{bpy})_2(\text{8-QPy})]^{2+}$ .<sup>112</sup> Efficient deactivation of the  $^3\text{MLCT}$  to close lying  $^3\text{MC}$  states of similar energy was indicated by calculations. However, isoenergetic  $^3\text{MLCT}$  and  $^3\text{MC}$  does not necessarily leads to rapid surface crossing. While the structurally related complex  $[\text{Ru}(\text{bpy})_2(\text{8-QPy})]^{2+}$  is weakly emissive at room temperature, the radiative rate constants are substantially higher than those of the QPz series.<sup>112</sup> The tridentate complex also displayed a very small radiative rate constant compared to

$[\text{Ru}(\text{tpy})_2]^{2+}$  ( $k_r$   $44 \times 10^3 \text{ s}^{-1}$ ).<sup>52</sup>  $[\text{Ru}(\text{dqp})_2]^{2+}$  on the other hand, displaying a  $k_r$  of  $7 \times 10^3 \text{ s}^{-1}$ , is more similar, which can be understood by their similar geometry; however, the difference in room temperature excited state lifetime is exceptionally large.<sup>52</sup>

While the very short Ru-N<sub>Pz</sub> bonds suggest large  $\sigma$ -donation, compared to that of Ru-N<sub>Q</sub>, this does not destabilize the <sup>3</sup>MC state enough to counter other effects. Additionally, the low emission energy suggests a shortening of the excited state lifetimes according to the energy gap law. Spectral component analysis revealed very large  $\nu_{1/2}$  compared to  $[\text{Ru}(\text{bpy})_3]^{2+}$  and similar complexes.<sup>123</sup> The broadening increases as the ground and excited state becomes more distorted.<sup>137</sup> This suggests a more distorted <sup>3</sup>MLCT state compared to the GS for  $[\text{Ru}(\text{Q1Pz})_3]^{2+}$  than for  $[\text{Ru}(\text{Q3PzH})_3]^{2+}$ , which can also be seen in the Ru-N<sub>Pz</sub> coordinate in the PPES, Figure 18.

The higher reactivity and lower selectivity of  $[\text{Ru}(\text{Q1Pz})_3]^{2+}$  can be ascribed to the substantially longer Ru-N<sub>Q</sub> bond in the <sup>3</sup>MC state,  $\sim 2.6 \text{ \AA}$ , compared to  $[\text{Ru}(\text{Q3PzH})_3]^{2+} \sim 2.4 \text{ \AA}$ . The difference in pyrazole orientation resulted in both markedly different electrochemical potentials, for both reduction and oxidation, as well as bond elongation in the <sup>3</sup>MC states, from TD-DFT calculations, both being important in photochemical experiments. The tridentate complex  $[\text{Ru}(\text{DQPz})_2]^{2+}$  displayed excellent photostability as well as dynamic room temperature diastereomerization, the latter which is not observed on NMR-time scales for the related complexes  $[\text{Ru}(\text{tpy})_2]^{2+}$  and  $[\text{Ru}(\text{dqp})_2]^{2+}$  due to a much lower (or rather lack of) and higher activation barrier. This dynamic behavior can have major implications for tridentate Ru<sup>II</sup> complexes in supramolecular chemistry.

## 5. Concluding remarks

The aim of my work has been to elucidate structure-function relationships in Ru<sup>II</sup> complexes, mainly with solar energy conversion applications in mind. For this purpose, the important aspects are mainly the absorption spectra, the redox chemistry and the excited state properties. Additionally, the photostability of the complex is important for any long-term application. From studying the three series of complexes, some important conclusions have emerged, which are summarized and put in context below.

It has been known for a long time that the structure of Ru<sup>II</sup> polypyridine complexes will affect its physical and chemical properties. This is easily seen in comparing pure pyridine and polypyridines in the homoleptic complexes [Ru(py)<sub>6</sub>]<sup>2+</sup>, [Ru(bpy)<sub>3</sub>]<sup>2+</sup> and [Ru(tpy)<sub>2</sub>]<sup>2+</sup>. All features six coordinated pyridines, but with substantially differing photophysical and photochemical properties. [Ru(py)<sub>6</sub>]<sup>2+</sup> is, apart from being problematic to synthesize, photolabile due to the monodentate ligand.<sup>18, 138</sup> [Ru(bpy)<sub>3</sub>]<sup>2+</sup> on the other hand display considerable absorption in the visible as well as long-lived <sup>3</sup>MLCT states (~1 μs) at room temperature. [Ru(tpy)<sub>2</sub>]<sup>2+</sup> also exhibit fair absorption but has, contrary to [Ru(bpy)<sub>3</sub>]<sup>2+</sup>, a very short excited state lifetime (~0.25 ns).<sup>18, 111</sup> The difference has largely been ascribed to the different geometries, where [Ru(bpy)<sub>3</sub>]<sup>2+</sup> is far more octahedral than [Ru(tpy)<sub>3</sub>]<sup>2+</sup>.<sup>111, 113</sup>

The bond in the 3,3-position of btx ligands and the chelation of the S-donor ligands leads to a distorted geometry compared to a perfect octahedron, while the structures of the QPz-complexes suggest much less distortion. Indeed, coordination of btc and PyS-Me in [Ru(bpy)<sub>2</sub>(btc)]<sup>2+</sup> and [Ru(N,N)<sub>2</sub>(PyS-Me)]<sup>2+</sup> perturb the diimine-chelation to different degrees. For the thioether, ~0.01 Å elongation of the Ru-N<sub>N,N</sub> bonds was observed, compared to [Ru(bpy)<sub>3</sub>]<sup>2+</sup>, while chelation of the btc-ligand display a minor trans-effect. The 3,3'-connection in btc results in an expanded bite-angle (82.5°), while the N-Ru-S bite-angles in [Ru(dmb)<sub>2</sub>(PyS-Me)]<sup>2+</sup> and [Ru(phen)<sub>2</sub>(PyS-Me)]<sup>2+</sup> are 82.0° and 84.0° respectively. Neither btc nor PyS-Me appear to cause major perturbation to the ancillary chelates, suggesting only minor inter-ligand steric interactions. For the QPz-series crystal structure and DFT calculations reveal that all complexes are very octahedral but with variations within the series, both in ground and excited states. The difference in coordination geometry, as calculated by DFT, between [Ru(Q3PzH)<sub>3</sub>]<sup>2+</sup> and [Ru(Q1Pz)<sub>3</sub>]<sup>2+</sup> shows that the orientation of the pyrazole in relation to the quinoline influences the coordination sphere, where the difference between the Ru-N<sub>Q</sub> and Ru-N<sub>Pz</sub> bond lengths was slightly larger for [Ru(Q3PzH)<sub>3</sub>]<sup>2+</sup>. The similar ground state geometries of the complexes suggest that the differences in the absorption spectra will be determined largely by electronic properties, not sterics.

An analysis of the absorption spectra of the complexes reveals, as expected, that the spectra are dependent on the hetero-atom coordinating to the metal. In general, the absorption maximum λ<sub>max</sub> is shifted to lower energies in the order: Ru-S=O, Ru-S, Ru-N, Ru-O=S. For Ru<sup>II</sup> complexes, the absorption maximum is often used as an estimate of the potential for the Ru<sup>2+/3+</sup> redox couple. However, the result presented in this thesis points out that these two do not correlate so well for QPz-complexes, not even within the series itself. A qualitative correlation was however evident for [Ru(N,N)<sub>2</sub>(PyS-Me)]<sup>2+</sup>, and the series [Ru(deeb)<sub>3</sub>]<sup>2+</sup> – O-

$[\text{Ru}(\text{deeb})_2(\text{PySO-}i\text{Pr})]^{2+} - [\text{Ru}(\text{deeb})_2(\text{PyS-}i\text{Pr})]^{2+} - \text{S-}[\text{Ru}(\text{deeb})_2(\text{PySO-}i\text{Pr})]^{2+}$ . This shows that the redox potentials and absorption does not always follow, even qualitatively, each other. Additionally, the large differences in both reduction and oxidation potentials between the bidentate QPz-complexes suggest that estimations to the oxidation potentials based on combination of ligands, such as Lever's electrochemical series,<sup>136</sup> must be applied with caution.

Light harvesting efficiencies and redox potentials are obviously very important properties for any molecule used in solar energy conversion schemes. However, the excited state properties are of greater importance, as the photochemistry occurs from this state, and determines whether the photon energy can be utilized. The difference in emissive properties at room temperature is strikingly clear between the heteroleptic complexes, where chelation of any btx ligand results in rapid decay of the <sup>3</sup>MLCT state via close lying <sup>3</sup>MC states, among other deactivation pathways. The large bite-angles in btx-complex are the main reason for the stabilization of the <sup>3</sup>MC states. In contrast,  $[\text{Ru}(\text{N,N})_2(\text{PyS-Me})]^{2+}$  are all emissive at room temperature, similar to, but less than the corresponding  $[\text{Ru}(\text{N,N})_3]^{2+}$ ; even though  $[\text{Ru}(\text{phen})_2(\text{PyS-Me})]^{2+}$  displays even wider bite-angles than  $[\text{Ru}(\text{bpy})_2(\text{btc})]^{2+}$ , in addition to long Ru-S bonds. It seems that the S-donor destabilized the <sup>3</sup>MC state enough to counter the effect of the less favorable coordination geometry. In the aspect of emission properties, the PyS-Me ligand has surprisingly small impact. The thioether complexes display no signs of photodegradation or ligand exchange reactions. This is in sharp contrast to  $[\text{Ru}(\text{deeb})_2(\text{PySO-}i\text{Pr})]^{2+}$  which exhibit non-reversible photoisomerization in acetonitrile. Since this behavior was not observed in the non-coordinating solvent propylene carbonate, it was attributed to ligand exchange reactions. Additionally, it is evident that the absorption spectra and electrochemical potentials can be shifted without significantly perturbing the emission spectra, as seen in  $[\text{Ru}(\text{N,N})_2(\text{PyS-Me})]^{2+}$  compared to  $[\text{Ru}(\text{N,N})_3]^{2+}$ ; as the absorption and the  $\text{Ru}^{3+/2+}$  and  $\text{Ru}^{2+/+}$  potentials typically report on the same states, where the emissive state is not involved.

While all QPz-complexes features a strong  $\sigma$ -bonding pyrazole and close to perfect octahedral geometry, the <sup>3</sup>MC states were all calculated to be downhill compared to the <sup>3</sup>MLCT surface, which has been predicted in calculations for emissive complexes as well.<sup>104</sup> The lack of room temperature emission in the QPz-complexes is due to a combination of fast non-radiative decay and very small radiative rate constants; where the geometrically similar, close to perfect octahedral, complexes  $[\text{Ru}(\text{DQPz})_2]^{2+}$  and  $[\text{Ru}(\text{dqp})_2]^{2+}$  both display  $k_r \sim 7 \times 10^3 \text{ s}^{-1}$ .<sup>52</sup> Similarly,  $[\text{Ru}(\text{bpy})_2(8\text{-QPy})]^{2+}$  display 3-8 times higher quantum yield at 77 K than the bidentate QPz-complexes.<sup>112</sup> While the radiative rates are similar with pyridine or pyrazole in the tridentate complexes, the non-radiative decay seems to be speeded up by the presence of the pyrazole. This clearly shows that the excited state properties cannot be explained only by geometric parameters in  $\text{Ru}^{\text{II}}$  complexes with polydentate ligands.

The spectral component analysis of the emission spectra at 77 K, reveals typical diimine localized <sup>3</sup>MLCT emission for  $[\text{Ru}(\text{deeb})_2(\text{btx})]^{2+}$  and  $[\text{Ru}(\text{N,N})_2(\text{PyS-Me})]^{2+}$ . However, these type of structured spectra, with clear vibrational progression, are not observed for the bidentate QPz-complexes, where the  $\nu_{1/2}$  values (1350-1480  $\text{cm}^{-1}$ ) are almost twice as large as for the studied heteroleptic complexes in the other two series. The large broadening masks the vibrational structure and the structure becomes further blurred by the higher frequency of the

low frequency accepting modes. The increase in  $\nu_{1/2}$  compared to  $[\text{Ru}(\text{bpy})_3]^{2+}$  ( $650 \text{ cm}^{-1}$ ) is observed for  $[\text{Ru}(\text{bpy})_2(8\text{-QPy})]^{2+}$  ( $1230 \text{ cm}^{-1}$ ) and  $[\text{Ru}(\text{bpy})_2(2\text{-QPy})]^{2+}$  ( $1040 \text{ cm}^{-1}$ ) as well, and is larger for the complex with the 6-membered chelate, ascribed to inter-ligand steric interactions.<sup>112</sup> The orientation of the quinoline-pyridine binding drastically changes the vibrational accepting modes, an effect also observed in chelation of the ligands in the QPz series which forms 6-membered chelates, where  $[\text{Ru}(\text{Q1Pz})_3]^{2+}$  displayed larger  $\nu_{1/2}$  compared to  $[\text{Ru}(\text{Q3PzH})_3]^{2+}$  by  $\sim 130 \text{ cm}^{-1}$ . The larger broadening indicated a large displacement between the ground and the emissive excited states.

The very large distortion in the  $^3\text{MC}$  states of these two complexes is responsible for the photo-reactivity. The distortion is especially pronounced in  $[\text{Ru}(\text{Q1Pz})_3]^{2+}$ , which is the main explanation for the increased photoinduced reactivity compared to  $[\text{Ru}(\text{Q3PzH})_3]^{2+}$ . The relatively minor structural difference between the ligands is of major importance for photochemical reactivity, pH sensitivity, and seemingly for the accessibility of empty Ru-coordination sites for photochemical applications. It is also evident that the S-to-O photo-induced linkage isomerization can be increased substantially (from 11% to 81%) by routine substitutions with electron withdrawing motifs on ancillary ligands, as observed when comparing  $[\text{Ru}(\text{bpy})_2(\text{PySO-}i\text{Pr})]^{2+}$  and  $[\text{Ru}(\text{deeb})_2(\text{PySO-}i\text{Pr})]^{2+}$ .<sup>77</sup> The lower O-to-S isomerization quantum yield in  $[\text{Ru}(\text{deeb})_2(\text{PySO-}i\text{Pr})]^{2+}$  further suggest that substitution with electron donating groups would instead increase  $\Phi_{\text{O}\rightarrow\text{S}}$ . Additionally, it is promising that the photoisomerization proceeded also when the complex is immobilized on  $\text{TiO}_2$  thin films, as the immobilization is a key feature in proposed molecular memory storage applications.

With all three series accounted for, a general picture of the complexes arise, where the functions are dependent on both geometric and electronic contributions. Seemingly subtle changes to one ligand can drastically alter the function of the complex. On the other hand, relatively major perturbation to the coordination sphere by one ligand does not necessarily result in largely perturbed functions. Consequently, the notion that  $\text{Ru}^{\text{II}}$  complexes with non-polypyridine ligands in general can be predicted by effects observed for the polypyridine complexes is in need of an update. The presented data in this thesis suggests a need to establish structure-function relationships for subsets of heterocyclic, polydentate non-polypyridine ligands, which I choose to call unconventional.



## 6. Acknowledgements

In this final piece of text, I would like to extend my sincerest gratitude to:

*Maria Abrahamsson* – My truly great advisor, I could not have wished for a better one. Not only that, but also a great friend. Thank you for all the innumerable discussions, advices, the knowhow, laughs and everything else! We have been a great team!

*Bo Albinsson* – My co-supervisor, for the spectroscopic knowhow and interesting discussions.

*All the collaborators* – I was fortunate enough to have veritable spectrum of collaborators (some 15 official ones), both near and far and all with expertise where I had little! I would like to thank you all for the work done and the progress we made!

*Magnus Bälter* – My coworker and, foremost, old friend. The time we met seems like a distant world at this point. Through thick and thin, high and low. What's next?

*All wonderful coworkers, previous and present* – For all the good times, the pleasant and helpful atmosphere. As it goes, none mentioned, none forgotten ... However, I would like to specifically thank Damir, Fredrik, Jesper, Maria, Mélina, Neda, Rita and Valeria. Also, a special thanks to the Monday group heroes, deciphering the science of seemingly impossible experiments.

*My family* – All of you, both my old and my new one. And especially so to my father, likely the reason I turned out so curious. I think I still beat you at chess, and I will win at wrestle, any day now ...

*My love and wife, Emelie* – Thank you for all your love, care and encouragement, and for our future together. I love you, and would not have managed this without you.

*With gratitude,  
Joachim Wallénstein*



## 7. References

1. J. Paris and W. W. Brandt, *J. Am. Chem. Soc.*, 1959, **81**, 5001-5002.
2. J. Demas and G. Crosby, *J. Mol. Spectrosc.*, 1968, **26**, 72-77.
3. F. E. Lytle and D. M. Hercules, *J. Am. Chem. Soc.*, 1969, **91**, 253-257.
4. D. Klassen and G. Crosby, *J. Chem. Phys.*, 1968, **48**, 1853-1858.
5. P. A. Mabrouk and M. S. Wrighton, *Inorg. Chem.*, 1986, **25**, 526-531.
6. E. M. Kober, B. P. Sullivan and T. J. Meyer, *Inorg. Chem.*, 1984, **23**, 2098-2104.
7. J. V. Caspar and T. J. Meyer, *J. Am. Chem. Soc.*, 1983, **105**, 5583-5590.
8. D. Klassen and G. Crosby, *Chem. Phys. Lett.*, 1967, **1**, 127-128.
9. A. Ceulemans and L. Vanquickenborne, *J. Am. Chem. Soc.*, 1981, **103**, 2238-2241.
10. C. Creutz, M. Chou, T. L. Netzel, M. Okumura and N. Sutin, *J. Am. Chem. Soc.*, 1980, **102**, 1309-1319.
11. E. M. Johansson, M. Odelius, S. Plogmaker, M. Gorgoi, S. Svensson, H. Siegbahn and H. Rensmo, *J. Phys. Chem. C*, 2010, **114**, 10314-10322.
12. A. M. Brown, C. E. McCusker and J. K. McCusker, *Dalton Trans.*, 2014, **43**, 17635-17646.
13. H. Yersin, W. Humbs and J. Strasser, *Coord. Chem. Rev.*, 1997, **159**, 325-358.
14. G. A. Crosby, *Acc. Chem. Res.*, 1975, **8**, 231-238.
15. K. R. Barqawi, A. Llobet and T. J. Meyer, *J. Am. Chem. Soc.*, 1988, **110**.
16. D. W. Thompson, A. Ito and T. J. Meyer, *Pure Appl. Chem.*, 2013, **85**, 1257-1305.
17. A. D. McNaught and A. D. McNaught, *Compendium of chemical terminology*, Blackwell Science Oxford, 1997.
18. A. Juris, V. Balzani, F. Barigelletti, S. Campagna, P. Belser and A. Von Zelewsky, *Coord. Chem. Rev.*, 1988, **84**, 85-277.
19. S. Campagna, F. Puntoriero, F. Nastasi, G. Bergamini and V. Balzani, in *Photochemistry and Photophysics of Coordination Compounds I*, Springer, 2007, pp. 117-214.
20. B. O'regan and M. Grätzel, *Nature*, 1991, **353**, 737-740.
21. S. Ardo and G. J. Meyer, *Chem. Soc. Rev.*, 2009, **38**, 115-164.
22. P. G. Bomben, K. C. Robson, B. D. Koivisto and C. P. Berlinguette, *Coord. Chem. Rev.*, 2012, **256**, 1438-1450.
23. R. C. Young, T. J. Meyer and D. G. Whitten, *J. Am. Chem. Soc.*, 1975, **97**, 4781-4782.
24. M. Grätzel, *Inorg. Chem.*, 2005, **44**, 6841-6851.
25. M. K. Nazeeruddin, C. Klein, P. Liska and M. Grätzel, *Coord. Chem. Rev.*, 2005, **249**, 1460-1467.
26. M. Grätzel, *Nature*, 2001, **414**, 338-344.
27. V. L. Gunderson, E. Krieg, M. T. Vagnini, M. A. Iron, B. Rybtchinski and M. R. Wasielewski, *J. Phys. Chem. B*, 2011, **115**, 7533-7540.
28. J. C. Freys, J. M. Gardner, L. D'Amario, A. M. Brown and L. Hammarström, *Dalton Trans.*, 2012, **41**, 13105-13111.
29. K. K.-W. Lo and S. P.-Y. Li, *RSC Advances*, 2014, **4**, 10560-10585.
30. S. Khatua, D. Samanta, J. W. Bats and M. Schmittel, *Inorg. Chem.*, 2012, **51**, 7075-7086.
31. J. W. Tucker and C. R. J. Stephenson, *J. Org. Chem.*, 2012, **77**, 1617-1622.
32. C. K. Prier, D. A. Rankic and D. W. C. MacMillan, *Chem. Rev.*, 2013, **113**, 5322-5363.

33. M. Hirahara, M. Z. Ertem, M. Komi, H. Yamazaki, C. J. Cramer and M. Yagi, *Inorg. Chem.*, 2013, **52**, 6354-6364.
34. J. J. Concepcion, J. W. Jurss, M. K. Brennaman, P. G. Hoertz, A. O. T. Patrocinio, N. Y. Murakami Iha, J. L. Templeton and T. J. Meyer, *Acc. Chem. Res.*, 2009, **42**, 1954-1965.
35. A. Lewandowska-Andralojc, D. E. Polyansky, R. Zong, R. P. Thummel and E. Fujita, *Phys. Chem. Chem. Phys.*, 2013, **15**, 14058-14068.
36. T. R. Cook, D. K. Dogutan, S. Y. Reece, Y. Surendranath, T. S. Teets and D. G. Nocera, *Chem. Rev.*, 2010, **110**, 6474-6502.
37. B. S. Howerton, D. K. Heidary and E. C. Glazer, *J. Am. Chem. Soc.*, 2012, **134**, 8324-8327.
38. J. D. Knoll, B. A. Albani, C. B. Durr and C. Turro, *J. Phys. Chem. A*, 2014, **118**, 10603-10610.
39. B. Happ, A. Winter, M. D. Hager and U. S. Schubert, *Chem. Soc. Rev.*, 2012, **41**, 2222-2255.
40. F. N. Castellano, *Acc. Chem. Res.*, 2015, **48**, 828-839.
41. H. Hofmeier and U. S. Schubert, *Chem. Soc. Rev.*, 2004, **33**, 373-399.
42. E. C. Constable, *Chem. Soc. Rev.*, 2007, **36**, 246-253.
43. M. Marcaccio, F. Paolucci, C. Paradisi, S. Roffia, C. Fontanesi, L. J. Yellowlees, S. Serroni, S. Campagna, G. Denti and V. Balzani, *J. Am. Chem. Soc.*, 1999, **121**, 10081-10091.
44. A. W. King, L. Wang and J. J. Rack, *Acc. Chem. Res.*, 2015, **48**, 1115-1122.
45. J. P. Sauvage, J. P. Collin, J. C. Chambron, S. Guillerez, C. Coudret, V. Balzani, F. Barigelletti, L. De Cola and L. Flamigni, *Chem. Rev.*, 1994, **94**, 993-1019.
46. D. L. Ashford, C. R. Glasson, M. R. Norris, J. J. Concepcion, S. Keinan, M. K. Brennaman, J. L. Templeton and T. J. Meyer, *Inorg. Chem.*, 2014, **53**, 5637-5646.
47. K. Nakamaru, *Bull. Chem. Soc. Jpn.*, 1982, **55**, 2697-2705.
48. V. Skarda, M. J. Cook, A. P. Lewis, G. S. McAuliffe, A. J. Thomson and D. J. Robbins, *J. Chem. Soc., Perkin Trans. 2*, 1984, 1309-1311.
49. A. Bencini and V. Lippolis, *Coord. Chem. Rev.*, 2010, **254**, 2096-2180.
50. M. A. Bork, H. B. Vibbert, D. J. Stewart, P. E. Fanwick and D. R. McMillin, *Inorg. Chem.*, 2013, **52**, 12553-12560.
51. T. Osterman, M. Abrahamsson, H.-C. Becker, L. Hammarström and P. Persson, *J. Phys. Chem. A*, 2012, **116**, 1041-1050.
52. M. Abrahamsson, M. Jäger, T. Österman, L. Eriksson, P. Persson, H.-C. Becker, O. Johansson and L. Hammarström, *J. Am. Chem. Soc.*, 2006, **128**, 12616-12617.
53. L. Hammarström and O. Johansson, *Coord. Chem. Rev.*, 2010, **254**, 2546-2559.
54. G. A. Parada, L. A. Fredin, M.-P. Santoni, M. Jäger, R. Lomoth, L. Hammarström, O. Johansson, P. Persson and S. Ott, *Inorg. Chem.*, 2013, **52**, 5128-5137.
55. M. R. Wasielewski, *Chem. Rev.*, 1992, **92**, 435-461.
56. F. De Angelis, S. Fantacci, A. Selloni, M. Grätzel and M. K. Nazeeruddin, *Nano Lett.*, 2007, **7**, 3189-3195.
57. T. Banerjee, A. K. Biswas, U. Reddy G, T. S. Sahu, A. Das, B. Ganguly and H. N. Ghosh, *J. Phys. Chem. C*, 2014, **118**, 3864-3877.
58. J. J. Concepcion, J. W. Jurss, M. R. Norris, Z. Chen, J. L. Templeton and T. J. Meyer, *Inorg. Chem.*, 2010, **49**, 1277-1279.
59. L. Duan, F. Bozoglian, S. Mandal, B. Stewart, T. Privalov, A. Llobet and L. Sun, *Nat. Chem.*, 2012, **4**, 418-423.
60. Y. M. Badiiei, D. E. Polyansky, J. T. Muckerman, D. J. Szalda, R. Haberdar, R. Zong, R. P. Thummel and E. Fujita, *Inorg. Chem.*, 2013, **52**, 8845-8850.

61. H.-W. Tseng, R. Zong, J. T. Muckerman and R. Thummel, *Inorg. Chem.*, 2008, **47**, 11763-11773.
62. G. A. Filonenko, D. Smykowski, B. M. Szyja, G. Li, J. Szczygieł, E. J. Hensen and E. A. Pidko, *ACS Catalysis*, 2015, **5**, 1145-1154.
63. A. J. Morris, G. J. Meyer and E. Fujita, *Acc. Chem. Res.*, 2009, **42**, 1983-1994.
64. R. Reithmeier, C. Bruckmeier and B. Rieger, *Catalysts*, 2012, **2**, 544-571.
65. W. Shockley and H. J. Queisser, *J. Appl. Phys.*, 1961, **32**, 510-519.
66. P. B. Arockiam, C. Bruneau and P. H. Dixneuf, *Chem. Rev.*, 2012, **112**, 5879-5918.
67. C. Gunanathan and D. Milstein, *Chem. Rev.*, 2014, **114**, 12024-12087.
68. H. A. Younus, W. Su, N. Ahmad, S. Chen and F. Verpoort, *Adv. Synth. Catal.*, 2015, **357**, 283-330.
69. S. Aiki, Y. Kijima, J. Kuwabara, A. Taketoshi, T.-a. Koizumi, S. Akine and T. Kanbara, *ACS Catalysis*, 2013, **3**, 812-816.
70. T. J. Seiders, D. W. Ward and R. H. Grubbs, *Org. Lett.*, 2001, **3**, 3225-3228.
71. S. Fanni, T. E. Keyes, C. M. O'Connor, H. Hughes, R. Wang and J. G. Vos, *Coord. Chem. Rev.*, 2000, **208**, 77-86.
72. F. Weisser, S. Plebst, S. Hohloch, M. van der Meer, S. Manck, F. Führer, V. Radtke, D. Leichnitz and B. Sarkar, *Inorg. Chem.*, 2015, **54**, 4621-4635.
73. A. A. Rachford, J. L. Petersen and J. J. Rack, *Inorg. Chem.*, 2006, **45**, 5953-5960.
74. A. A. Rachford and J. J. Rack, *J. Am. Chem. Soc.*, 2006, **128**, 14318-14324.
75. J. J. Rack, A. A. Rachford and A. M. Shelker, *Inorg. Chem.*, 2003, **42**, 7357-7359.
76. D. P. Butcher, A. A. Rachford, J. L. Petersen and J. J. Rack, *Inorg. Chem.*, 2006, **45**, 9178-9180.
77. B. A. McClure and J. J. Rack, *Angew. Chem. Int. Ed.*, 2009, **48**, 8556-8558.
78. J. J. Rack, *Coord. Chem. Rev.*, 2009, **253**, 78-85.
79. E. N. Dixon, M. Z. Snow, J. L. Bon, A. M. Whitehurst, B. A. DeGraff, C. Trindle and J. N. Demas, *Inorg. Chem.*, 2012, **51**, 3355-3365.
80. A. K. McEvoy, C. M. McDonagh and B. D. MacCraith, *Analyst*, 1996, **121**, 785-788.
81. A. Pyle, J. Rehmann, R. Meshoyrer, C. Kumar, N. Turro and J. K. Barton, *J. Am. Chem. Soc.*, 1989, **111**, 3051-3058.
82. E. Schrödinger, *Phys. Rev.*, 1926, **28**, 1049.
83. N. J. Turro, *Modern molecular photochemistry*, University science books, 1991.
84. W. T. Silfvast, *Laser fundamentals*, Cambridge University Press, 2004.
85. H. B. Gray, *J. Chem. Educ.*, 1964, **41**, 2.
86. J. R. Lakowicz, *Principles of fluorescence spectroscopy*, Springer Science & Business Media, 2013.
87. A. Jablonski, *Nature*, 1933, **131**, 21.
88. M. T. Hassan, T. T. Luu, A. Moulet, O. Raskazovskaya, P. Zhokhov, M. Garg, N. Karpowicz, A. Zheltikov, V. Pervak and F. Krausz, *Nature*, 2016, **530**, 66-70.
89. D. S. McClure, *J. Chem. Phys.*, 1949, **17**, 905-913.
90. J. C. Koziar and D. O. Cowan, *Acc. Chem. Res.*, 1978, **11**, 334-341.
91. M. Kasha, *Discuss. Faraday Soc.*, 1950, **9**, 14-19.
92. N. S. Lewis and D. G. Nocera, *PNAS*, 2006, **103**, 15729-15735.
93. D. Gust, T. A. Moore and A. L. Moore, *Acc. Chem. Res.*, 2009, **42**, 1890-1898.
94. J. J. Rack and N. V. Mockus, *Inorg. Chem.*, 2003, **42**, 5792-5794.
95. N. Tamai and H. Miyasaka, *Chem. Rev.*, 2000, **100**, 1875-1890.
96. P. F. Barbara, T. J. Meyer and M. A. Ratner, *J. Phys. Chem.*, 1996, **100**, 13148-13168.
97. R. A. Marcus, *J. Chem. Phys.*, 1956, **24**, 966-978.
98. N. Hush, *Trans. Faraday Soc.*, 1961, **57**, 557-580.
99. J. Miller, L. Calcaterra and G. Closs, *J. Am. Chem. Soc.*, 1984, **106**, 3047-3049.

100. C. J. Timpson, C. A. Bignozzi, B. P. Sullivan, E. M. Kober and T. J. Meyer, *J. Phys. Chem.*, 1996, **100**, 2915-2925.
101. J. K. McCusker, *Acc. Chem. Res.*, 2003, **36**, 876-887.
102. A. C. Bhasikuttan, M. Suzuki, S. Nakashima and T. Okada, *J. Am. Chem. Soc.*, 2002, **124**, 8398-8405.
103. J. V. Caspar and T. J. Meyer, *Inorg. Chem.*, 1983, **22**, 2444-2453.
104. M. Abrahamsson, M. J. Lundqvist, H. Wolpher, O. Johansson, L. Eriksson, J. Bergquist, T. Rasmussen, H.-C. Becker, L. Hammarström and P.-O. Norrby, *Inorg. Chem.*, 2008, **47**, 3540-3548.
105. E. M. Kober, J. V. Caspar, R. S. Lumpkin and T. J. Meyer, *J. Phys. Chem.*, 1986, **90**, 3722-3734.
106. J. V. Caspar and T. J. Meyer, *J. Phys. Chem.*, 1983, **87**, 952-957.
107. M. J. Cook, A. P. Lewis, G. S. McAuliffe, V. Skarda, A. J. Thomson, J. L. Glasper and D. J. Robbins, *J. Chem. Soc., Perkin Trans. 2*, 1984, 1303-1307.
108. Y. Sun, M. El Ojaimi, R. Hammitt, R. P. Thummel and C. Turro, *J. Phys. Chem. B*, 2010, **114**, 14664-14670.
109. J. A. Treadway, B. Loeb, R. Lopez, P. A. Anderson, F. R. Keene and T. J. Meyer, *Inorg. Chem.*, 1996, **35**, 2242-2246.
110. B. H. Farnum, J. J. Jou and G. J. Meyer, *PNAS*, 2012, **109**, 15628-15633.
111. M. Maestri, N. Armaroli, V. Balzani, E. C. Constable and A. M. C. Thompson, *Inorg. Chem.*, 1995, **34**, 2759-2767.
112. M. Abrahamsson, H.-C. Becker, L. Hammarström, C. Bonnefous, C. Chamchoum and R. P. Thummel, *Inorg. Chem.*, 2007, **46**, 10354-10364.
113. D. G. Brown, N. Sangantrakun, B. Schulze, U. S. Schubert and C. P. Berlinguette, *J. Am. Chem. Soc.*, 2012, **134**, 12354-12357.
114. A. B. Tamayo, B. D. Alleyne, P. I. Djurovich, S. Lamansky, I. Tsyba, N. N. Ho, R. Bau and M. E. Thompson, *J. Am. Chem. Soc.*, 2003, **125**, 7377-7387.
115. A. J. Metherell, W. Cullen, A. Stephenson, C. A. Hunter and M. D. Ward, *Dalton Trans.*, 2014, **43**, 71-84.
116. A. Yeh, N. Scott and H. Taube, *Inorg. Chem.*, 1982, **21**, 2542-2545.
117. K. Garg, A. W. King and J. J. Rack, *J. Am. Chem. Soc.*, 2014, **136**, 1856-1863.
118. A. J. Bard, L. R. Faulkner, J. Leddy and C. G. Zoski, *Electrochemical methods: fundamentals and applications*, Wiley New York, 1980.
119. R. S. Lumpkin and T. J. Meyer, *J. Phys. Chem.*, 1986, **90**, 5307-5312.
120. S. A. Chabolla, E. A. Dellamary, C. W. Machan, F. A. Tezcan and C. P. Kubiak, *Inorg. Chim. Acta*, 2014, **422**, 109-113.
121. A. Staniszewski, W. B. Heuer and G. J. Meyer, *Inorg. Chem.*, 2008, **47**, 7062-7064.
122. W. B. Heuer, H.-L. Xia, W. Ward, Z. Zhou, W. H. Pearson, M. A. Siegler, A. A. Narducci Sarjeant, M. Abrahamsson and G. J. Meyer, *Inorg. Chem.*, 2012, **51**, 3981-3988.
123. L. Hammarström, F. Barigelletti, L. Flamigni, M. T. Indelli, N. Armaroli, G. Calogero, M. Guardigli, A. Sour, J.-P. Collin and J.-P. Sauvage, *J. Phys. Chem. A*, 1997, **101**, 9061-9069.
124. J. Breu and A. J. Stoll, *Acta Crystallogr. Sect. C: Cryst. Struct. Commun.*, 1996, **52**, 1174-1177.
125. N. A. Al-Rawashdeh, S. Chatterjee, J. A. Krause and W. B. Connick, *Inorg. Chem.*, 2013, **53**, 294-307.
126. B. A. McClure, Ohio University, 2010.
127. T. Kojima, T. Morimoto, T. Sakamoto, S. Miyazaki and S. Fukuzumi, *Chem. Eur. J.*, 2008, **14**, 8904-8915.

128. H. B. Kim, N. Kitamura and S. Tazuke, *J. Phys. Chem.*, 1990, **94**, 7401-7405.
129. R. Ballardini, A. Credi, M. T. Gandolfi, F. Marchioni, S. Silvi and M. Venturi, *Photochem. Photobiol. Sci.*, 2007, **6**, 345-356.
130. S. Bonnet and J.-P. Collin, *Chem. Soc. Rev.*, 2008, **37**, 1207-1217.
131. N. Koumura, R. W. Zijlstra, R. A. van Delden, N. Harada and B. L. Feringa, *Nature*, 1999, **401**, 152-155.
132. J. J. Rack, J. R. Winkler and H. B. Gray, *J. Am. Chem. Soc.*, 2001, **123**, 2432-2433.
133. A. W. King, Y. Jin, J. T. Engle, C. J. Ziegler and J. J. Rack, *Inorg. Chem.*, 2013, **52**, 2086-2093.
134. K. Garg, S. I. Paris and J. J. Rack, *Eur. J. Inorg. Chem.*, 2013, **2013**, 1142-1148.
135. S. Ardo, Y. Sun, F. N. Castellano and G. J. Meyer, *J. Phys. Chem. B*, 2010, **114**, 14596-14604.
136. A. J. Canty and C. V. Lee, *Organometallics*, 1982, **1**, 1063-1066.
137. B. A. McClure, E. R. Abrams and J. J. Rack, *J. Am. Chem. Soc.*, 2010, **132**, 5428-5436.
138. J. L. Templeton, *J. Am. Chem. Soc.*, 1979, **101**, 4906-4917.